HHS Public Access

Author manuscript

Cell Rep. Author manuscript; available in PMC 2025 May 24.

Published in final edited form as:

Cell Rep. 2025 April 22; 44(4): 115450. doi:10.1016/j.celrep.2025.115450.

Hi-C profiling in tissues reveals 3D chromatin-regulated breast tumor heterogeneity informing a looping-mediated therapeutic avenue

Lavanya Choppavarapu[1,2,3,5], **Kun Fang**[1,2,3,5], **Tianxiang Liu**[1,2,3], **Aigbe G. Ohihoin**[4], **Victor X. Jin**[1,2,3,6,*]

[1]Divison of Biostatistics, Data Science Institute, Medical College of Wisconsin, Milwaukee, WI 53226, USA

[2]MCW Cancer Center, Medical College of Wisconsin, Milwaukee, WI 53226, USA

[3]Mellowes Center for Genomic Sciences and Precision Medicine, Medical College of Wisconsin, Milwaukee, WI 53226, USA

[4]Cell and Developmental Biology PhD program, Medical College of Wisconsin, Milwaukee, WI 53226, USA

SUMMARY

The limitations of Hi-C (high-throughput chromosome conformation capture) profiling in *in vitro* cell culture include failing to recapitulate disease-specific physiological properties and lacking a clinically relevant disease microenvironment. In this study, we conduct Hi-C profiling in a pilot cohort of 12 breast tissues comprising two normal tissues, five ER+ breast primary tumors, and five tamoxifen-treated recurrent tumors. We demonstrate 3D chromatin-regulated breast tumor heterogeneity and identify a looping-mediated target gene, CA2, which might play a role in driving tamoxifen resistance. The inhibition of CA2 impedes tumor growth both *in vitro* and *in vivo* and reverses chromatin looping. The disruption of CA2 looping reduces tamoxifen-resistant cancer cell proliferation, decreases CA2 mRNA and protein expression, and weakens the looping interaction. Our study thus provides mechanistic and functional insights into the role of 3D chromatin architecture in regulating breast tumor heterogeneity and informs a new looping-mediated therapeutic avenue for treating breast cancer.

In brief

*Correspondence: vjin@mcw.edu.
[5]These authors contributed equally
[6]Lead contact

AUTHOR CONTRIBUTIONS

V.X.J. conceived the project. L.C. conducted the experiments. K.F. performed the data analyses. T.L. assisted with the data analysis. A.G.O. assisted with the experiments. V.X.J., L.C., K.F., T.L., and A.G.O. wrote the manuscript.

DECLARATION OF INTERESTS

The authors declare no competing interests.

SUPPLEMENTAL INFORMATION

Supplemental information can be found online at https://doi.org/10.1016/j.celrep.2025.115450.

Choppavarapu et al. find that a looping-mediated CA2 plays a role in driving tamoxifen resistance. The inhibition of CA2 impedes tumor growth and reverses chromatin looping, while the disruption of CA2 looping reduces cancer cell proliferation, as well as decreasing CA2 mRNA and protein expression, and weakens the looping interaction.

Graphical Abstract

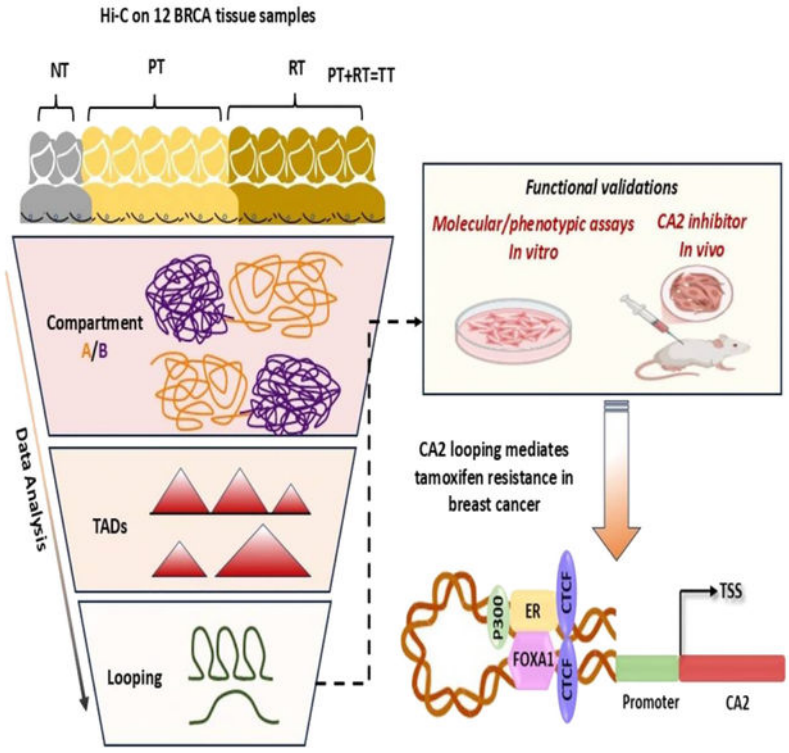

INTRODUCTION

Endocrine therapy, including tamoxifen (Tam), is currently a standard and effective treatment for estrogen receptor-α-positive (ER+) breast cancer patients.[1] However, about one-third of all ER+ breast cancer patients eventually develop treatment resistance to this hormonal therapy and many even die from this cancer.[2,3] Current treatment strategy is mainly guided by breast cancer patient prognosis with a typical pathological risk assessment.[4,5] Such treatment selection generally doesn't consider individual patient tumor genomic heterogeneity. Recent studies on characterizing the genomic landscape of breast patient cohorts have revealed the molecular differences among individual breast tumors, including genomic drivers of breast cancer progression, intra- or intertumoral heterogeneity, and the variable responses of individual patients to therapies associated with these molecular differences.[6–10] Despite these genomic studies of patient cohorts having provided insights into the biological underpinnings of this cancer, the limitation was that they were mainly focused on copy number and gene expression analyses. Therefore, it is imperative to

examine intra- or intertumoral heterogeneity on a three-dimensional (3D) genome scale and to determine the differences in 3D chromatin architecture in breast cancer patient cohorts.

Current knowledge of 3D chromatin regulation in normal and disease states was mostly accumulated through Hi-C (high-throughput chromosome conformation capture) profiling in *in vitro* cell culture systems.[11–16] Although these cell model studies have been very useful in unraveling the alterations in 3D-regulated biological pathways in diseases, such studies as many other cell line studies clearly showed many limitations, including failing to recapitulate disease-specific physiological properties and, often, lacking a clinically relevant disease microenvironment. A few recent studies not only adapted the Hi-C technique to human patient samples but also revealed patient- or tumor-subtype-specific 3D genome architecture.[17–20] For example, Xu et al. identified AML (acute myeloid leukaemia) subtype-specific changes in 3D genome features such as compartments, topologically associated domain (TAD) boundaries, and chromatin loops and further showed that repressive loops were widespread in the genome.[17] Johnstone et al. identified an intermediate compartment between the open A and the closed B compartments that shifted its interactions toward the B compartment in colorectal tumors.[18] Kloetgen et al. highlighted 3D landscape variations among different leukemia subtypes and suggested that drugs with reported antileukemic activity partially reversed 3D interactions in specific loci.[19] However, studies of the 3D chromatin landscape in breast cancer patients are lacking. It is becoming very clear that to expand the characterization of 3D genome organization in breast cancer patient samples is an emerging task. Such studies would advance a novel concept that the variable response of individual breast cancer patients to endocrine therapy is governed by individual tumor (IT)-specific 3D chromatin domains, a clear departure from the prevailing paradigm that endocrine treatment responses are driven by genetic variability among patients. This thus motivates us to conduct this study to elucidate 3D-chromatin-regulated breast cancer heterogeneity.

In this study, we conduct a tissue-specific Hi-C profiling[21] in a pilot cohort of 12 breast tissues comprising 2 normal tissues (NTs) and 10 ER+ breast tumors (TTs), including 5 primary tumors (PTs) and 5 Tam-treated recurrent tumors (RTs). Here, we identify differential chromatin compartments among NTs, PTs, and RTs, as well as PT-, RT-, and IT-specific TADs and looping genes. We also cross-examine the interplay among the three layers of 3D chromatin structure. We further overlay tumor-derived looping genes and cell-derived looping genes to obtain common looping genes and then perform *in silico* analyses to identify novel looping-mediated biological pathways that might mediate resistance to endocrine therapy. We test the efficacy of an inhibitor targeting metabolism pathways in *in vitro* cell lines and *in vivo* cell-line-derived xenografts (CDXs) and conduct chromosome conformation capture (3C)/real-time qPCR validations. Finally, we employ the CRISPR-Cas9 technique to delete the CA2 enhancer looping region *in vitro* to assess its causal relationship in mediating endocrine resistance. Therefore, our study yields significant mechanistic and functional insights into the role and clinical relevance of 3D chromatin architecture in breast cancer endocrine resistance.

RESULTS

Compartments are largely preserved among breast tumors

To comprehensively examine the variability of 3D chromatin architecture in breast tumor tissues, we conducted tissue-specific Hi-C profiling in a pilot cohort comprising two NTs, five PTs, and five RTs (Table S1) and produced a total of 4 billion raw pair-end reads with an average of ~350 million per tissue (Figure S1). We then performed computational analyses to interrogate the interplay of three layers of chromatin architecture in a tumor-specific manner (Figure 1A). We first applied HiC-Pro[22] to identify the A/B compartments for each individual tissue and found that there were roughly the same number (~2,000) of compartments for all 12 tissues and a nearly even number of compartments A and B within each of the 12 tissues, where a majority of the compartments were less than 2 Mb in size (Figure 1B). We then used dcHiC[23] to identify differential compartments between TTs and NTs (TTs vs. NTs) and between RTs and PTs (RTs vs. PTs) (Table S2). Interestingly, we found that 2,085 and 391 bins of 100 kb/bin were differential compartments at a false discovery rate (FDR) <0.1 for TTs vs. NTs and RTs vs. PTs, respectively (Figure 1C), indicating that the compartment patterns were largely conserved among tumor tissues but exhibited a greater disparity between tumor tissues and NTs. We further classified those differential compartment bins into flipping transitions, i.e., A to B or B to A, and matching transitions, i.e., A to A or B to B. Of all differential compartment bins between TTs and NTs, 79.6% (46.8% NT A to TT B and 32.8% NT B to TT A) were flipping transitions and 20.4% were matching transitions (Figures 1D, top, and S2A). Interestingly, we found that the B-A flipping transition was more dominant in the PT to RT transition, such that 73.7% (15.3% PT A to RT B and 58.3% PT B to RT A) were flipping transitions and 26.3% were matching transitions (Figures 1D, bottom, and S2b). An example of identified flipping and matching transitions for TTs vs. NTs and RTs vs. PTs was visualized by Integrative Genomics Viewer (IGV) (Figures 1E, S2C, and S2D). Finally, we leveraged a quantile-normalized principal-component analysis (STAR Methods) to calculate compartment similarities within (intra-) or among (inter-) tissues. We found that the intratissue correlations were generally larger than the intertissue correlations, and the RT-PT correlation was higher than the PT-NT and RT-NT correlations (Figure 1F). Taken together, our results demonstrated that 3D chromatin architecture at the compartment layer was largely preserved among breast tumor tissues, with a small percentage of chromatin regions undergoing compartment flipping during the progression of breast cancer endocrine resistance.

TADs are highly heterogeneous among breast tumors

Next, we wanted to examine the tumor-specific chromatin architecture at the TAD layer. We used TopDom[24] to identify ~6,000 TADs for each of 12 tissues (Figures 2A, left, and S3A) and observed similar size distributions of TADs across the tissues (Figure 2A, right). To identify tumor-specific TADs among multiple tissues in various groups, we developed a computational algorithm, Group- and Individual-Sample-Specific TADs (GISTA), which enables us to compare TADs among various groups of tissues as well as at the individual tissue (STAR Methods and Figure S3B). In the group-level comparison, GISTA was able to define three categories of TAD changes: intertumor conserved TADs

(C-TADs), intertumor moderately variable TADs (MV-TADs), and intertumor significantly variable TADs (SV-TADs) (STAR Methods, Figures S3C and S3D, and Table S3). In the individual-level comparison, GISTA further subclassified those SV-TADs into two types of IT-specific TADs: highly IT-specific (HS) TADs and lowly IT-specific (LS) TADs. GISTA also identified three special types of IT-specific TAD changes: neo (N)-deletion (D), split (S)-fused (F), and mixed (coexistence of both ND and SF).

After applying GISTA in our pilot, we identified 2,751 TAD arrays with most of the sizes of arrays ranging from 0.1 to 10 Mb (Figure 2B). We found that 1,134 (41.3%) of them were C-TADs, 1,094 (39.8%) were MV-TADs, and 521 (19.0%) were SV-TADs between TTs and NTs (Figures 2C and S3E), whereas 1,130 (41.1%) were C-TADs, 1,081 (39.3%) were MV-TADs, and 538 (19.6%) were SV-TADs between RTs and PTs (Figures 2D and S3E). Interestingly, we found that the size of the TAD arrays in SV-TADs was larger than those in MV-TADs and C-TADs for both TTs vs. NTs and RTs vs. PTs (Figure S4A). We also observed much more HS types than LS types correlatively with ND, SF, and mixed, with 356 and 166 in TTs vs. NTs and 442 and 97 in RTs vs. PTs, respectively (Figures 2C and 2D). Moreover, mixed type constituted a majority (>50%) of TAD changes in both TTs vs. NTs and RTs vs. PTs comparisons. As expected, we found a more diverse occurrence of N/D/S/F types within HS type for each tissue than within LS type (Figures 2E, S4B, and S4C). As visualized in Figure 2F for two examples, one falling under the LS-N of SV-TADs category on chromosome 1 and the other under the HS-F of SV-TADs category on chromosome 20, we illustrated the TAD changes among the ITs. In sum, we identified tumor-specific TAD changes and demonstrated a highly heterogeneous TAD change among breast tumors.

Chromatin loops are intensively variable among breast tumors

Chromatin looping is a key layer of 3D chromatin architecture that brings distal regulatory elements such as enhancers into proximity with promoters of target genes and has been shown to be linked to Tam resistance in breast cancer cell lines.[13,25] To identify looping events in tumor tissues and tumor-specific looping genes, we first used FitHiC2[26] to identify a range of ~100,000–140,000 interacting loci and an average of ~25,000 promoter (P)-distal (D) loops per tissue, where an interacting locus was annotated as a P-D loop such that one end of interacting locus is at the promoter region of a UCSC RefSeq gene and the other is within the distal region (200 kb upstream/downstream of the 5′ transcription start site [TSS]) of the same gene (Figures 3A and S5A). A gene with at least one P-D loop was further defined as a looping gene. There was an average of ~12,000 looping genes per tissue (Figure S5B). We then calculated a gene-based looping intensity (LI) by combining all P-D loops associated with a particular gene across all 12 tissues (STAR Methods and Figure S5C). We then performed a bi-Gaussian modeling on the Euclidean distance of LI between each two of 10 TTs and 2 NTs (Figure S5D) to define TT-specific differential looping genes (DLGs), including gained (GLGs) or lost looping genes (LLGs) based on the sign of the distance. We identified a range of 1,326–1,895 GLGs and a range of 1,049–1,792 LLGs for each of 10 TTs (Figures 3B and S5E). Remarkably, we observed a negative correlative trend that the number of shared GLGs or LLGs was decreasing along with the increase in the number of shared tumors (Figure 3C), suggesting looping genes are quite

diverse among ITs. In parallel, we identified a range of 1,189–1,668 GLGs and a range of 427–607 LLGs (Figures 3D and 3E) for each of five RTs. We also observed a similar trend that the number of shared GLGs or LLGs was decreasing along with the increase in the number of shared RTs (Figure 3F and Table S4). Bird's-eye views of a few GLGs, CA2, NUBPL, and ATP2B2, are shown in Figures 3G and S5F. Collectively, our results revealed intensively variable chromatin looping events among individual breast tumors, suggesting a looping-mediated tumor heterogeneity during the progression to endocrine resistance.

Cross-examination identifies RT-specific looping-mediated biological pathways

We further conducted a qualitative comparison among the set of RT-specific DLGs (5,877 gained and 1,869 lost), four differential compartments (A-A, A-B, B-A, and B-B), and six types of SV-TADs (HS-ND, HS-SF, HS-mixed, LS-ND, LS-SF, and LS-mixed) (Figure 4A). We observed that the number of looping genes associated with differential compartments was substantially lower than those associated with TAD changes. This might primarily be due to the fact that compartment segments at a 100-kb bin-size resolution instead of the whole compartment were considered as differential by dcHiC. Interestingly, a positive correlation was identified between individual HS TADs and DLGs (Figure 4B). To explore a correlation of the three layers of chromatin architecture with copy number variations (CNVs), we further performed an analysis by applying HiNT[27] on tissue Hi-C data and identified numerous CNVs, including copy number gain, loss, and neutral variants (Figures S6A, S6B, and S6C). We discovered a higher percentage of overlap between compartments and copy number gain/loss in tumor tissues (Figure S6D). Additionally, we also observed that the contact frequency within TAD boundaries around the CNV breakpoints was notably low[16] (Figure S6E), and the total number of loops located in copy number gain/loss regions was greater in RTs than in PTs (Figure S6F).

We next cross-examined the tumor-specific DLGs with the cell-based DLGs. We first used the same method of analyzing tumor-based Hi-C data to reanalyze the Hi-C data on the three breast cancer cell systems, MCF7 vs. MCF7TR, T47D vs. T47DTR, and ZR75–1 vs. ZR75–1TR, from our previous study.[28] We thus obtained TR-specific DLGs for each of the three cell systems. We then overlapped each of the three TR-specific DLGs with the set of ≥1RT RT-specific DLGs and found that the common looping genes among different sets were quite diverse (Figure 4C). For example, for the overlapping of GLGs with RT1–5, MCF7TR had 216 GLGs with RT1 and T47DTR had 204, 225, 228, and 235 GLGs with RT2 to RT5, respectively, while ZR75–1TR had mild overlapping with all RTs compared to MCF7TR and T47DTR. For the overlapping of LLGs with RT1–5, MCF7TR had 125, 85, 122, and 99 LLGs with RT1, RT2, RT3, and RT5, respectively, while T47DTR had mild overlapping with all RTs compared to MCF7TR and ZR75–1TR, and ZR75–1TR had the most overlapping with RT3. We further derived the differentially expressed looping genes (DELGs) by correlating common DLGs with differentially expressed genes (DEGs) for MCF7/MCF7TR and T47D/T47DTR cells. We identified a total of 68 DELGs, including 35 gained/upR, 21 lost/downR, 6 gained/downR, and 6 lost/upR, for MCF7/MCF7TR as well as a total of 115 DELGs, including 54 gained/upR, 21 lost/downR, 31 gained/downR, and 9 lost/upR (Figure S7A). Furthermore, we performed gene ontology (GO) and biological pathway analyses by using DAVID[29] and Enrichr.[30] For MCF7TR-specific

DELGs, we found reversible hydration of carbon dioxide, interferon-gamma-mediated signaling pathway, and bicarbonate transport to be among the top enriched pathways under GO and REACTOME analyses and amino acid metabolism, nitrogen metabolism, and Wnt signaling pathway under KEGG and WIKI analyses (Figure 4D). The results of GO, REACTOME, KEGG, and WIKI analyses on T47DTR-specific DLGs are shown in Figure S7B. Surprisingly, there were very few common pathways between two cell systems, including RNA stabilization, bicarbonate transport, and nitrogen metabolism, in which these pathways encompass nine MCF7TR-specific DELGs, AXIN2, CA1, CA2, C4BPA, C4BPB, CBLB, DDO, DTD2, and IL7R and seven T47DTR-specific DELGs, AQP1, CA1, CA2, COX6C, HMGCS1, TP63, and UQCR10. Since CA1 and CA2 are common between MCF7TR and T47DTR, we subsequently performed survival analyses[31] on these two genes and found that higher expression levels of both genes were associated with a worse relapse-free survival in breast cancer patients treated with Tam (Figures 4E and S7C). We examined the distal loops of both CA1 and CA2 with the enrichment of various transcription factors (TFs) and histone marks compared with our previously published data. We found a higher enrichment of ER, FOXA1, P300, H3K4me3, H3K4me1, H3K27ac, CTCF, and ATAC-seq signals but lower enrichment of H3K27me3 in the CA2 distal loop in MCF7TR vs. MCF7 cells (Figure 4F) and higher enrichment of H3K4me1, H3K27ac and CTCF in the CA1 distal loop in MCF7TR vs. MCF7 cells (Figure S7D). Remarkably, our single-cell RNA sequencing (scRNA-seq) data and scATAC-seq data conducted in a separate cohort of breast tumor tissues demonstrated a higher expression of CA2 and higher open chromatin signals in three RTs vs. three PTs (Figure 4G). Our data thus strongly support the notion that an enhancer-promoter looping (EPL)-mediated CA2 might play a role in driving Tam resistance. Together, our analysis results identified RT-specific looping-mediated biological pathways by cross-examining tumor-based and cell-based DLGs.

The inhibition of CA2 impedes tumor growth both *in vitro* and *in vivo*

Numerous previous studies have demonstrated that CA2 plays an important role in tumor progression, metastasis, and treatment resistance.[32–36] Our comprehensive analysis not only suggested a role for EPL-mediated CA2 in contributing to Tam resistance, but also pinpointed it as a promising therapeutic target gene. Brinzolamide, a commercially available inhibitor targeting CA2, has been tested for its antitumor activities in glioblastoma and blood cancer.[37,38] We thus attempted to test its inhibition efficacy in Tam-resistant breast cancer cells by using both *in vitro* phenotypical assays and an *in vivo* CDX mouse model.

We first applied the CCK-8 assay to evaluate the effect of brinzolamide on MCF7/MCF7TR and T47D/T47DTR cell growth and to determine their respective optimal inhibitor concentrations over a 0- to 6-day period (Figures S8A and S8B). We observed a stronger inhibition of cell growth or impedance of cell proliferation in both TR cells than in two Tam-sensitive (TS) cells, MCF7 and T47D, respectively (Figures 5A and 5B). We then tested brinzolamide's therapeutic efficacy in CDXs by utilizing MCF7 and MCF7TR cells in estrogen-disk-implanted female nu/nu mice. Following the development of palpable tumors, the mice were administered either brinzolamide or a control solution for a 5-week period. Notably, the MCF7TR CDXs in the brinzolamide-treated group exhibited a significantly slower tumor growth rate compared to those in the control group (Figure 5C), whereas

MCF7 CDXs did not show any significant decrease in tumor growth rate (Figure S8C). Crucially, throughout the treatment and post-treatment periods, the mice showed no signs of drug-induced toxicity, and there were no substantial weight differences between the treated and the control groups for both CDX models (Figures 5D and S8D). After the mice reached the predetermined tumor burden as per the protocol, all mice were euthanized, and the mammary tumors were excised. Tumors from brinzolamide-treated MCF7TR CDXs were significantly smaller than those from the control group, a pattern not seen in MCF7 CDXs (Figures 5E, S8E, S9A, and S9B). Our findings from both *in vitro* and *in vivo* functional characterization underscore the therapeutic potential of targeting CA2 in treating Tam-resistant breast cancer.

The inhibition of CA2 reverses chromatin looping

To assess whether the inhibition of CA2 might alter the chromatin looping and gene expression of CA2 itself, as well as other looping-mediated TR-specific genes within the transport and metabolism pathways, we conducted 3C-qPCR and real-time qPCR analyses on selected genes in MCF7/MCF7TR and T47D/T47DTR cells. Upon treatment with brinzolamide, we observed a significantly decreased EPL interaction of CA2 in both MCF7TR and T47DTR cells, in contrast to their respective TS cells (Figures 6A and 6B). Additionally, brinzolamide led to diminished EPL interactions for other looping genes, including CA1, AXIN2, C4BPA, CBLB, IL7R, DDO, and DTD2 in MCF7TR cells and CA1, COX6C, TP63, and HMGCS1 in T47DTR cells (Figures 6A and 6B). These results indicated that brinzolamide was able to reverse chromatin looping activities. The gene expression level showed a reversed expression of CA2 between MCF7 and MCF7TR, as well as between T47D and T47DTR cells (Figures 6C and 6D). However, this reversal of expression was not so evident for some other genes in the TR cells. Nevertheless, our data revealed a mechanistic link between looping-mediated CA2 and the transport and metabolism pathways in promoting breast cancer cell Tam resistance. In summary, the silencing of CA2 through pharmacological drug inhibition is able to reverse the chromatin looping of CA2 and some other RT-specific looping genes, suggesting CA2 might play an oncogenic role in driving the progression of breast cancer endocrine resistance through a chromatin looping mechanism.

To determine whether the CA2 EPL causally regulates TR breast cancer cell growth, we employed CRISPR-Cas9 technology to delete a 4-kb CA2 enhancer looping region (chr8:86,446,013–86,450,019) in MCF7TR cells and generated a CRISPR knockout (KO) MCF7TR cell subline. We observed a significant reduction in cell growth in CRISPR KO cells compared to MCF7TR wild-type (WT) cells. Interestingly, treatment with 4-hydroxytamoxifen (4-OHT), the active metabolite of Tam, had minimal impact on cell proliferation in both WT and CRISPR KO cells (Figure S10A). 3C-qPCR, real-time qPCR, and western blotting analyses showed an ~80% reduction in the interaction frequency (Figure S10B), a significant decrease in CA2 transcript levels (Figure S10C) and a reduction in CA2 protein expression (Figure S10D) in CRISPR KO cells compared to WT controls, demonstrating the causal role of this EPL in controlling CA2 gene transcription and further regulating TR breast cell proliferation. Collectively, these results indicate that the CA2 EPL

is a key mediator of breast cancer Tam resistance, highlighting its potential as a therapeutic target in overcoming endocrine resistance.

DISCUSSION

Despite many studies having linked alterations in 3D chromatin organization to cancer development and treatment resistance,[15,28,39–43] including breast cancer endocrine resistance,[15,41,42] most of these studies were conducted in cancer cell culture models, except for a few very recent studies conducted in human tumor samples.[17–20] Those Hi-C studies in tumor samples clearly revealed very sophisticated 3D genome regulatory patterns, including inter- and intratumor heterogeneity. To this end, we designed this study to exploit the 3D chromatin variation in a pilot of 12 breast normal and tumor tissues. Our comprehensive analysis of the three layers of chromatin architecture uncovered intertumor heterogeneities among breast tumors in all of three layers, compartment, TAD, and chromatin looping. Furthermore, our cross-examination of tumor-based looping genes and cell-based looping genes identified the common looping genes enriched in the transport and nitrogen metabolism pathway. Of the gained looping and upregulated genes within this metabolism pathway, CA2 showed a worse relapse-free survival in breast cancer patients treated with Tam (Figure 4F), indicating its potential oncogenic role in driving the progression of breast cancer endocrine resistance. Indeed, a pharmacological inhibition of CA2 showed a trend toward reduced tumor growth both *in vitro* and *in vivo* (Figure 5). Due to a small cohort size in our xenograft study, further validation in larger, more statistically powered studies is needed to confirm these findings. Nevertheless, our study advances a novel concept that endocrine-treatment responses could be governed by IT-specific 3D chromatin domains, which clearly departs from the prevailing paradigm that endocrine-treatment responses are driven by the genetic variability between individual patients. Therefore, this work will yield significant mechanistic and functional insights into the role and clinical relevance of 3D chromatin architecture in breast cancer endocrine resistance.

Our data demonstrate a conserved compartmentalization in terms of the size and number of A/B compartments across breast tumors, a finding consistent with other studies in leukemia and colon cancer.[17,18] Our data also suggest that chromatin architecture is largely preserved at the compartment layer. However, TADs, another layer of chromatin architecture, were highly heterogeneous among breast tumors. Due to a lack of computational tools available for identifying TAD variability across groups of tumor samples or within ITs, we developed GISTA, a novel algorithm tailored to identify SV-TADs among different groups of multiple samples. The novelty of GISTA includes (1) comparing the difference between two groups based on a series of TADs arrays instead of individual TAD, (2) applying dynamic programming to capture the boundary of a TAD array with a user-defined boundary-shift parameter, and (3) utilizing a decision tree to annotate different types of TAD changes. To evaluate our tool, we benchmarked GISTA against TADCompare (STAR Methods), a widely used tool for detecting differential boundaries between two conditions, and observed a comparable performance between the two methods (Figures S11A–S11G). In addition, we were able to apply our GISTA on Hi-C data in a colon cancer cohort[18] and to recapitulate the previous findings. Together, these data demonstrated the efficiency and the reliability of GISTA (Figure S11H).

To assess the reliability of the identified TADs, we performed an aggregated TAD analysis (ATA) on all TADs and demonstrated that TADs identified at 40 kb resolution were reliable under the current sequencing depth (Figure S12A). Using GISTA, we identified various subtypes of SV-TADs, including conserved and PT- or RT-specific TADs, demonstrating the tool's versatility and applicability in analyzing chromatin variability across two or more tumor groups. We then performed pathway enrichment analyses for subtypes of SV-TADs in the comparisons of TTs vs. NTs and RTs vs. PTs (Figures S12B and S12C). We observed that the Hippo signaling pathway, steroid hormone biosynthesis, and cell cycle were among the most enriched pathways in TTs vs. NTs, consistent with findings from previous studies.[44–46] Interestingly, nitrogen metabolism, including CA2, was enriched in both TTs vs. NTs and RTs vs. PTs, suggesting that this pathway may be involved in regulating cell adaptive plasticity during oncogenesis and Tam resistance. Moreover, BMP and MAPK signaling pathways were enriched in SV-TADs from RTs vs. PTs, in line with our recent single-cell sequencing findings.[47] Additionally, Wnt and HIF-1 signaling pathways highlighted in the analysis were reported to be associated with poor prognosis and Tam-resistant breast cancer.[48,49] Of note, we also performed the evaluation of the robustness of interaction loci and chromatin loops using APA (aggregate peak analysis) (Figure S12D).

While it has been documented that breast cancer cell-specific chromatin looping plays a crucial role in regulating the expression of oncogenes,[50,51] a comprehensive understanding of the chromatin looping variability in Tam resistance is still lacking. Remarkably, we observed that the common DLGs (both gained and lost) among tumors decrease with the increase in the number of shared tumors (Figure 3C). A similar trend was also observed in RTs (Figure 3F). The extensive variabilities in chromatin looping across tumors, especially in RTs, highlight an important role of chromatin looping in regulating breast tumor heterogeneity. We also found a positive correlation of DLGs with HS TADs but not with differential compartments, which could be possibly explained by the model of TAD formed through a loop extrusion,[52–54] whereas compartments are formed by a distinct mechanism.[55] Despite other studies suggesting that the variations in the intrinsic chromatin interaction landscape were associated with differential gene expression,[56] our data demonstrated a low correlation between differential chromatin looping genes with differential gene expression. Nevertheless, from the set of RT-specific DELGs, we were able to identify several interesting signaling pathways, including RNA stabilization, bicarbonate transport, and nitrogen metabolism, which might be involved in regulating Tam resistance.

Notably, we identified CA2, an enzyme of the family of carbonic anhydrases (CAs), as a potential driver in the progression of Tam resistance. CAs facilitate the conversion of CO_2 and H_2O into bicarbonate, playing vital roles in diverse cellular processes.[37,57] Although previous work has linked the expression of CA2 with patient survival rates in luminal B breast cancer,[58] its role in Tam-resistant breast cancer remains unexplored. Our functional examination demonstrated that CA2 inhibition impeded cell proliferation in MCF7TR and T47DTR cells as well as slowing tumor growth in xenograft mouse models upon treatment with a CA2-specific inhibitor, brinzolamide.[59–61] Furthermore, we showed reversible chromatin looping and gene expression of CA2 and other genes in TR cells after CA2 inhibition, suggesting CA2 might play an oncogenic role in driving Tam resistance through a chromatin looping mechanism. Nevertheless, additional experiments are needed

to elucidate the underlying mechanism of how looping-mediated CA2 regulates downstream biological pathways and further drives Tam resistance.

We propose a possible looping-mediated mechanistic model for driving breast cancer Tam resistance: in PTs or TS cells, looping-mediated pathways and their component genes are inactive due to their weakened enhancer-promoter (E-P) interactions, while in Tam-treated RTs or Tam-resistant cells, these E-P interactions are strengthened, leading to activation of genes and pathways (Figure 6E). Our model is further substantiated by the following observations: increased chromatin accessibility and active histone marks (H3K4me1 and H3K27ac), along with strengthened binding of ER, FOXA1, P300, and CTCF, while the repressive mark H3K27me3 was decreased in the CA2 enhancer region in MCF7TR compared to MCF7 cells (Figures 4G and 6E). We thus hypothesize that CA2 is silenced by the loss of ER signaling[62] in TS breast cancer cells. A prolonged Tam treatment mediates a non-genomic calcium signaling, resulting in activation of kinase pathways such as MAPK/ERK, which can modulate the ER in the cell membrane to translocate to the nucleus and promote CA2 activation through a looping regulation. This non-genomic and genomic crosstalk can in turn enhance cell migration and proliferation,[63] resulting in Tam resistance. Future experiments will test this hypothesis with various functional and molecular assays, such as CRISPR-Cas9, 3D-fluorescence *in situ* hybridization (FISH), and 3C/chromatin immunoprecipitation (ChIP)/real-time qPCR.

In summary, our study has produced a rich resource of high-quality 3D chromatin data in a pilot cohort of tumor tissues, in which they can further be used for identifying 3D chromatin guided prognostic biomarkers to stratify breast cancer that may acquire resistance to endocrine therapy and subsequently designing more effective therapeutic strategies to overcome Tam resistance. To the best of our knowledge, this is the first investigation of 3D chromatin variabilities in breast tumor tissues, and our study provides a mechanistic insight into the role of 3D-chromatin-regulated breast tumor heterogeneity as well as informing a new looping-mediated therapeutic avenue for treating breast cancer.

Limitations of the study

It is important to acknowledge that our study has several limitations that warrant consideration. First, the sequencing depth of our Hi-C data (80M–175M valid pairs) is below the optimal resolution, particularly for loop detection at fine scales. More specifically, this limitation may impact the ability to detect proximal loops, such as E-P interactions within 20 kb. We addressed this by validating the robustness of our analyses through ATA and APA, by cross-referencing with comparable studies (Figure S12), and by *in vitro* and *in vivo* experimental validations. However, a deeper sequencing would likely enhance the resolution and allow for the identification of finer chromatin features. Second, our pilot cohort size, particularly the inclusion of only two NT samples, limits the generalizability of the findings and introduces potential confounders, such as age discrepancies between normal and tumor samples and age-related epigenetic and chromatin organization differences. While this study was primarily aimed at testing the feasibility of our approach, future studies with expanded, age-matched cohorts will allow us to systematically assess these factors and determine whether the observed trends are broadly applicable or age specific. Despite these limitations,

our study nevertheless provides a valuable resource of 3D genome organization in breast cancer and could serve as a baseline for further investigations with higher-resolution data and larger sample sizes.

RESOURCE AVAILABILITY

Lead contact

Requests for further information and resources should be directed to and will be fulfilled by the lead contact, Victor Jin (vjin@mcw.edu).

Materials availability

This study did not generate new unique reagents.

Data and code availability

Raw and processed Hi-C data for tissue samples were deposited in GEO under accession no. GSE261230. Other public datasets analyzed during the current study are available in the GEO repository: GEO: GSE144380,[28] GSE108787,[15] GSE128676,[28] and GSE128460.[64]

The source codes of this study are freely available at GNU General Public License (GPL-v.3.0) (https://github.com/KunFang93/TumorSpecific3DChromatinDomain).

STAR★METHODS

EXPERIMENTAL MODEL AND STUDY PARTICIPANT DETAILS

A total of twelve human breast normal and tumor tissue samples were used for the study. Five fresh primary and five fresh tamoxifen-treated recurrent breast tumor samples were purchased from Bay Biosciences LLC (Brookline, MA). Two normal breast tissues were procured from National Disease Research Interchange (NDRI, Philadelphia) as fresh frozen pieces (Table S1). All breast tumors are ER +, aged between 45 and 70 years old, grade between G1 and G3. All the tissues were stored at −80°C until they were used for experiments. The use of breast normal and tumor tissues for this study was conducted under MCW approved IRB approval. All tissues were subjective to Hi-C profiling and data analysis.

METHOD DETAILS

Hi-C profiling on breast tissues: Approximately 100–200 mg of each tissue was chopped into fine pieces before being fixed. Hi-C was performed using Phase Genomics Proximo Hi-C kits v4.0 (Phase genomics, Seattle, WA) according to the manufacturer's instructions.[21] Briefly, the finely chopped tissues were incubated with crosslinking solution for 15 minutes with gentle rotation. Tissue lysis was performed with motor and pestle with liquid nitrogen and grinded to a fine powder and resuspended in 700 μl of Lysis buffer 1. The chromatin containing supernatant was pelleted and washed with 500 μl of 1x CRB, resuspended in 100 μl of Lysis Buffer 2. 100 μl of SPRI beads were added, incubated and washed with 200 μl of 1x CRB. SPRI beads containing chromatin were resuspended in 150 μl of fragmentation buffer, 5 μl of restriction enzyme (Sau3AI) and incubated at 37 °C for 1

hour. 2.5 μl of finishing enzyme is added and mixed by vortexing. Ligation was performed by adding 95 μl of Ligation buffer and 5 μl ligation enzyme to the SPRI beads containing chromatin. To revert the crosslinking, 5 μl of RX enzyme was added to the reaction and then incubated overnight at 65 °C with shaking (900 rpm). The pellet was washed, air dried, resuspended in 100 μl of elution buffer and then incubated for 5 minutes at room temperature. The beads were washed and resuspended in 100 μl of bead binding buffer. After the final wash the beads were resuspended in 200 μl of deionized water and measured the concentration of DNA using Qubit dsDNA HS assay kit. About 500 ng of streptavidin beads containing DNA were separated, resuspended in 20 μl of deionized water, and a total of 25 μl of library reagent and an approximate amount of library reagent 1 is added. The reaction was mixed gently and incubated at 55 °C for 10 min. PCR was performed by adding 26 μl of HSR mix (PCR Hotstart Ready mix) and 5 μl of PCR index primer to each reaction. After the amplification, the sample was size selected by adding 25 μl of SPRI beads to the library. The beads were separated and washed twice with 200 μl of 80% ethanol for at least 30 sec each and the pellet was air dried for no longer than 5 min at room temperature. The beads were resuspended and separated and the supernatant containing the final Hi-C library which was quantified using Qubit dsDNA HS assay kit on a Qubit. The library was sequenced on Illumina HiSeq3000.

Cell lines and reagents: Human breast cancer cell lines MCF7, T47D and their tamoxifen resistant (TR) cells were derived from previous studies.[72–75] Both MCF7 and T47D cells were cultured in RPMI1640 medium (Thermo Fisher Scientific, Catalog #A1049101) supplemented with 10% fetal bovine serum (FBS) (Thermo Fisher Scientific, Catalog # SH30071.03) and 1% Penicillin-Streptomycin (Thermo Fisher Scientific, Catalog # 15140122). Tamoxifen resistant cells were cultured in phenol-red free RPMI1640 medium (Thermo Fisher Scientific, Catalog # 11835030) with 10% charcoal-stripped FBS (Thermo Fisher Scientific, Catalog # 50–165-7328) and 1% Penicillin-Streptomycin and 100nM tamoxifen (Sigma-Aldrich, Catalog #H7904–5MG). Tamoxifen was replaced every 48h. All the cells were grown at 37°C and 5% CO2 until they reach 90% confluence. The cells were treated with Brinzolamide (Selleckchem, Catalog # S3178). The gradient concentrations of Brinzolamide are 1μM for MCF7 cells and 5mM for T47D cells respectively. Cell absorbance was recorded at different time points.

CCK-8 cell viability assay: Cell viability was measured by CCK-8 (CCK-8, Dojindo, USA) assay following the manufacturer's instruction. In brief, MCF7, T47D and their tamoxifen resistant (TR) cells were harvested and plated at a density of 1×10^3 cells per well in 96-well plates (Corning Inc) and cultured in an incubator5% CO2 incubator at 37 °C. After 24 h the culture media was replaced, and the cells are incubated with various concentrations of Brinzolamide. At the end of each time point 10 μL of CCK-8 solution was added to each 96-well plates and the mixture was incubated for 1 hour in the incubator at 37 °C. The optical density at 450 nm was measured at different time points using BioTek ELx800 Absorbance Microplate reader.[28] The experiments were repeated and analyzed three times separately.

RNA isolation and RT-qPCR: Total RNA was isolated using Quick -RNATM Mini Prep (Zymo Research, USA) according to the manufacturer's instructions. Five million cells from MCF7 and MCF7TR were lysed in RNA lysis buffer followed by eliminating the majority of gDNA with Spin-Away Filter. Then the mixture of RNA and ethanol was loaded onto Zymo-Spin IIICG Column followed by DNase I treatment to remove the traces of DNA. The samples are washed twice with RNA wash buffer and the total RNA was eluted in 50μL DNase/RNase-Free Water. Two microgram of RNA was used to convert to cDNA using a high-capacity cDNA reverse transcription Kit (Applied Biosystem). qPCR was conducted with a Power SYBRTM Green PCR Master mix (Applied Biosystem). Real-time qPCR was performed on QuantStudio 3 Real-Time PCR system (Applied Biosystem, USA) according to the manufacturer's instructions. The relative expression of RNAs was determined by the ΔΔCT method using ACTB as an internal control for quantification analyses of gene targets.[28,64] Primers used are listed in (Table S5). Each PCR reaction was performed in triplicate, and the data presented were the average of three independent experiment results for all PCR reactions.

3C-qPCR: 3C-qPCR experiment was performed as previously described.[76] Approximately five to ten million cells of MCF7, T47D and their TR cells were cross-linked with 1% formaldehyde for 10 min at room temperature. The reaction was quenched by 1 M glycine for 5 min at room temperature. Cells were lysed with 500μl of cold lysis buffer (10 MmTris–HCl Ph 8.0, 10 Mm NaCl, 0.2% Igepal CA630) with protease inhibitors for 1 h on ice. After lysis, the cell nuclei were pelleted, and the chromatin was digested using 200 units of HindIII (NEB) at 37 °C overnight and then the digestion was stopped with 1.6% SDS at 65 °C for 20 min. Digested DNA fragments were ligated using T4 DNA ligase (NEB) for 4 h at 16 °C. Samples were reverse cross-linked with Proteinase K at 65 °C overnight. 3C samples were then purified using phenol–chloroform extraction. The 3C template was dissolved in 10 mM Tris-HCl and DNA concentrations were measured using Nanodrop. For3C several primers are designed for a restriction fragment of interest. All 3C primers were designed by "Primer 3". Primers used are listed in (Table S6). Interactions were measured using a 3C-qPCR assay for ligation products between each anchor HindIII fragment and each target HindIII fragment. Results are presented as relative interaction frequencies compared with those GAPDH as an internal control.[28,76,77] After PCR, the frequency of the ligation events was estimated through agarose gel electrophoresis.

***In* vivo Xenograft mouse model:** Female 6-week-old nude mice were used. All protocols were IACUC approved, and all the mice experiments were conducted at Rincon Biosciences (Utah). Subcutaneous implantation of 17β-Estrogen pellets (0.72 mg, 60-day release; Innovative Research of America) was performed on the same day as cell injection in 6-week-old female immune-deficient nude mice. The mice were inoculated subcutaneously with 1×10^6 cells of either MCF7 or MCF7TR cells, suspended in equal volumes of PBS and Matrigel. Once tumors became palpable, their sizes were measured every three days, and the tumor volume was calculated using the following formula: tumor volume (mm^3) = length × $width^2$ × 0.5. Upon reaching a mean size of approximately 150–250 mm^3, the MCF7 and MCF7TR xenograft mice were randomly allocated into two groups, each consisting of six mice: (1) control group (treated with vehicle corn oil), (2) Brinzolamide

(Selleckchem) group (oral administration at 50 mg/kg, three times a week). The data collected from this study encompassed animal weights, observations, and tumor dimensions. The data were utilized to assess drug tolerability, weight variations and gross physiological changes, as well as to evaluate anticancer activity through tumor growth inhibition or regression. Tumor volumes were monitored until the mice were euthanized. The mice were euthanized humanely, and their tumors were subsequently collected and stored for further studies. A two-way ANOVA mixed model with Dunnett's test was performed to analyze tumor growth data, ensuring robust and statistically significant results.

CRISPR/Cas9 deletion: Genomic deletion of the CA2 enhancer looping region in MCF7TR cells was achieved using the CRISPR/Cas9 system.[78] Single-guide RNAs (sgRNAs) were designed to target specific sequences within the CA2 enhancer looping region and were synthesized as per established protocols. The sgRNAs were transfected into MCF7TR cells via **nucleofection** using the program optimized for these cells. The PCR products were used to validate the deletion of the target distal region of CA2, and the sequences were analyzed by Sanger sequencing. Successful knockout was verified through PCR and sequencing of the target locus. All sgRNA sequences used in this study are provided in (Table S7). Post-transfected cells were cultured under selective conditions, and clones were isolated for further characterization. For 4hydroxytamoxifen (4-OHT, Millipore sigma) experiments, 5μM of 4-OHT was added to MCF7TR WT and CRISPR KO cells.[47]

Western blotting: MCF7TR WT and MCF7TR CRISPR KO cells were seeded in six-well plates at a density of 2×10^5 cells per well. Once the cells reached 90–100% confluence, they were lysed using cold RIPA lysis buffer (Pierce; Thermo Fisher Scientific, USA). The protein concentration was determined with the BCA Protein Assay kit (Pierce; Thermo Fisher Scientific, USA). On 12% SDS-PAGE, 25 μg of protein were separated and then transferred onto a polyvinyl difluoride (PVDF) membrane (Bio-Rad, USA). Membranes were then blocked with 5% bovine fetal serum at room temperature for 1 h. The membranes were subsequently incubated with primary antibodies at 4 °C overnight followed by secondary antibody for 1 h at room temperature. The blots were developed with detected by enhanced chemiluminescence detection kit (Bio-Rad Laboratories Inc.). The band intensity was quantified using NIH Image-J software (National Institutes of Health, Bethesda, MD, USA).[47,79,80] Primary antibodies used were CA2 (Proteintech, cat. no. 16961–1-AP, 1:500) and β-actin (Cell signaling, cat.no. 4967S, 1:1000). Horseradish peroxidase conjugated secondary antibodies against rabbit (cat. no. 656120; 1:5000) were purchased from Invitrogen.

Differential compartments analysis: We used HiC-Pro[22] to process the raw Hi-C data to generate the raw contact matrices with 100kb resolution for all tissue samples. The raw contact matrices were then fed into dcHiC[23] to detect the compartment A/B and the differential compartments. Briefly, raw principal component (PC) files for each chromosome were first created by dcHiC and the best PCs within PC1 and PC2 were selected by comparing the correlation of each one against GC content and gene density. Then, the selected PCs were quantile normalized by calculating the Mahalanobis distance. Finally, four differential compartments were detected based on the normalized PCs, including two

compartment transitions A-B and B-A from NTs to TTs and PTs to RTs; and the overall correlations of compartments among NTs, PTs and RTs were computed based on calculated quantile normalized PCs with a customized python script. IGV was used to visualize the compartment.

Tumor-specific TADs analysis: We utilized HiC-Pro to process the raw Hi-C data to generate the iced contact matrices with different resolutions, including 20k, 40k, 100k and 150k, for all tissue samples. We then applied TopDom[24] to call TADs for all resolutions with a series of window sizes (only parameter for TopDom), 5, 8, 10, 13 and 15. We selected the best parameters win 5, resolution 40k for TopDom based on the number of TADs and the size of TADs reported in the previous literatures[24,81] (Figure S2). ATA was performed by GENOVA.[66] Since current existed tools[71,82–85] for identifying differential TADs have several drawbacks, including only allowing a comparison of two samples, providing no specific types of TAD changes, and missing the comparison between TAD to Gap or Boundary, we developed a novel algorithm, GISTA, to detect TAD changes across multiple samples. GISTA is composed of three steps: 1). Partitioning the whole genome into a series of TADs arrays across all samples; 2). Constructing a feature vector for each TADs array; 3). Annotating the type of TAD change to each TADs arrays and statistical inference. The detailed method is the following:

We denoted the sample m in nth group as $G_k \,.\, I_m k \in 1,\ 2\cdots, K$ and M$m \in 1, 2\cdots,$.

1. Partitioning the whole genome into a series of TADs arrays across all samples: We applied a dynamic programming approach to identify the 'preserved' borders across all samples, allowing a small pre-threshold shift (default 2 bins) based on the TAD's resolution. Then, those borders are used to partition the whole genome into a series of TADs array, noted by $1TA_i,\ i\ =\ 1,\ 2, \ldots, l;\ I\ =\ the\ number\ of\ borders\ +$.

2. Constructing a feature vector for each TADs array: We constructed two feature matrices for TA_i: Neo-Del score matrix (denoted as ND_i) and Split-Fuse score matrix (denoted as SF_i). We defined $nd_{r,c}$ and $sf_{r,c}(r, c \in \{G_1 \,.\, I_1, \cdots, G_k \,.\, I_m\})$ as the notes for the elements in ND_i and SF_i. Before calculating $nd_{r,c}$ and $sf_{r,c}$, we first built a length dictionary L_i, and a sign dictionary S_i. The keys in L_i and S_i are samples (denoted as $s \in \{G_1 \,.\, I_1, \cdots, G_k \,.\, I_m\}$); and values are denoted as A_i^s and B_i^s, which are the length vector and the sign vector of TA_i for s, respectively. Each array element a in A_i^s is the binsize-scaled TAD's length, calculated by

$$a = \frac{End_{T|G|B}\ -\ Start_{T|G|B}}{Binsize}$$

(Equation 1)

And each array element b in B_i^s is measured by

$$b = \begin{cases} \dfrac{End_T - Start_T}{Binsize} \\ -\dfrac{End_{G,B} - Start_{G,B}}{Binsize^2} \end{cases}$$

(Equation 2)

where T, G, B represent TAD, Gap and Boundary respectively, binsize is the resolution of Hi-C that used to identify TADs. Then, for element $nd_{r,c}$ in ND matrix, it is then calculated by

$$nd_{r,c} = \sum S_i[c] - \sum S_i[r]$$

(Equation 3)

For element $sf_{r,c}$ in SF matrix, it is then calculated by

$$idx = \min(\|L_i[c]\|, \|L_i[r]\|),$$

(Equation 4)

$$\Delta_{r,c} = \left| \sum Sort(L_i[c])_{1:idx} - \sum Sort(L_i[r])_{1:idx} \right|,$$

(Equation 5)

$$sf_{r,c} = Sign(\|L_i[c]\| - I\|L_i[r]\|) * \Delta_{r,c}$$

(Equation 6)

where $Sort$ represents descending sort function and $Sign$ represents sign function. We finally converted ND_i and SF_i to a feature vector (denoted as V_i) based on arithmetic mean of the pre-setting groups. For example, in this study, we have three groups, NTs, PTs, and RTs with two, five, five tumor samples, $G_{NT} \subseteq (G_{NT}.I_1, G_{NT}.I_2)$, $G_{PT} \subseteq (G_{PT}.I_1 \cdots G_{PT}.I_5)$, $G_{RT} \subseteq (G_{RT}.I_1 \cdots G_{RT}.I_5)$ and we are interested in finding the G_{TT}-specific TADs ($G_{PT,RT}$ vs G_{PT}), then feature vector in this case contains the following elements: $[ND_{G_{NT}}^{G_{PT,RT}}, SF_{G_{NT}}^{G_{p\tau,RT}}, ND_{G_{NT}}^{G_{NT}}, SF_{G_{NT}}^{G_{NT}}, ND_{G_{PT,RT}}^{G_{p,RT}}, SF_{G_{PT,RT}}^{G_{pT,RT}}]$, where the subscript indicates the selected columns and the superscript indicates the select rows in the ND or SF. For example, $ND_{G_{NT}}^{G_{PT,RT}}$ is the arithmetic mean of $2ND_{rows,cols}, rows \in (G_{PT}.I_1, \cdots, G_{RT}.I_5),\ cols \in (G_{NT}.I_1, G_{NT}.I)$.

3. Annotating the type of TAD changes and statistical inference: We first row-wise concatenated all V_i to build a feature matrix, F, For the previous example $G_{PT,RT}$ *vs* G_{PT}, the rows in F represent TADs arrays and columns are, $SF_{G_{NT}}^{G_{PT,RT}}, ND_{G_{NT}}^{G_{NT}}, SF_{G_{NT}}^{G_{NT}}, ND_{G_{PT,RT}}^{G_{PT,RT}}, SF_{G_{PT,RT}}^{G_{PT,RT}}$.

We then converted F to F_{LMH} by categorizing the elements in F into 'L(ow)', 'M(edium)' and 'H(igh)' categories. Detailly, we set $Q_{ND}(0.1)$ and $Q_{ND}(0.7)$ of the $F_{I,ND}$, as well as $Q_{SF}(0.1)$ and $Q_{SF}(0.7)$ of the $F_{I,SF}$ as the cutoff for 'L' and 'H', and elements besides 'L' and 'H' are 'M' (Extended Data Figure 3C). In the previous example, $F_{I,ND}$ and $F_{I,SF}$ are extract from F by selecting ND and SF related columns separately:

$$F_{ND} = F\left[:, \left(ND_{G_{NT}}^{G_{PT,RT}}, ND_{G_{NT}}^{G_{NT}}, ND_{G_{PTT,RT}}^{G_{PT,RT}}\right)\right],$$

(Equation 7)

$$F_{SF} = F\left[:, \left(SF_{G_{NT}}^{G_{PT,RT}}, SF_{G_{NT}}^{G_{NT}}, SF_{G_{PT,RT}}^{G_{PT,RT}}\right)\right]$$

(Equation 8)

We then applied decision trees (Figure S3D) to annotate each TADs array to obtain distinct types of TAD changes including 'Inter-tumor conserved TADs' (C-TADs), 'inter-tumor moderately variable TADs' (MV-TADs) and 'inter-tumor significantly variable TADs' (SV-TADs) based on F_{LMH}. C-TADs refers to TADs that are consistent across two groups, MV-TADs refers to TADs that exhibit mild variations between two groups, and SV-TADs refers to TADs with significant variations between two groups. (Figure S3F). We further defined six subtypes of changing within SV-TADs, which composed of the combinatorial of two individual-sample level changes, 'individual high-specific' (HS) and 'individual low-specific' (LS), as well as three TAD type changes, N(eo)D(eletion), S(plit) F(usion) and Mixed (NDSF) from F_{LMH}. Specifically, HS are TA_i that categorized as high in either $ND_{G_T}^{G_T}$ or $SF_{G_T}^{G_T}$, G_T represent Test groups and LS the complementary set of HS. ND are TA_i only categorized as high in $ND_{G_C}^{G_T}$, SF are TA_i only categorized as high in $SF_{G_C}^{G_T}$ and Mixed are the rest TAs, G_C represents Control groups.

Finally, we performed a permutation test to infer the statistical significance of Group-Variation-H based on F, we first built the observations with

$$obs = \left(ND_{G_C}^{G_T} + SF_{G_C}^{G_T}\right) - c^*\left(ND_{G_C}^{G_C} + SF_{G_C}^{G_C}\right) - t^*\left(ND_{G_T}^{G_T} + SF_{G_T}^{G_T}\right)$$

(Equation 9)

Where c and t is calculated from $argmax(||obs < 0.05||)$, $c, t \in \{0.1n, 0 \leq n \leq 10, n \in \mathbb{Z}\}$. Then the observations were permutated 1000 times. And the p values were represented by the proportion of the permutated observation that are more extreme than actual observations. The visualization of N/D/S/F scaled frequency and TADs was implemented by Logomaker[65] and GENOVA,[66] respectively.

Evaluation of GISTA: We benchmarked the GISTA with TADCompare.[71] As the TADCompare was designed for pairwise differential boundary detection, we first generated aggregated raw contact matrices for five PTs and five RTs and normalized the aggregated contact matrices using ICE with HiC-Pro. TADs of aggregated samples were then

called using TopDom with the same parameters (win5, resolution 40kb). We then used TADCompare to detect differential boundaries with its default parameters. As GISTA originally was designed for multisample comparison, we expanded GISTA's functionality on detecting differential TADs arrays between two samples by making pseudo-replicates with adapted the core algorithm described above. Finally, customized scripts were used to compare results from TADCompare and GISTA.

Looping genes analysis: The interacting loci were identified by FitHiC2[26] with the parameters -r 20000 -L 40000 -x intraOnly -U 1000000. We filtered out the low interacting loci with contact counts under the 0.98 quantile of all interacting loci's contact counts. We assessed the robustness of the detected interacting loci and chromatin loops by aggregated peaks analysis from GENOVA[66]. The remaining interacting loci with high contact counts were further screened out with their genomic locations. Specifically, we defined a P-D loop as one end of an interacting loci on the promoter region of a RefSeq protein-coding gene and the other end on the distal region of the same gene. The promoter region of a gene was defined as from 4 kilobases (kb) upstream of 5'TSS to 2 kb downstream of 5'TSS. The distal region of a gene was defined as 200 kb to 10 kb upstream and downstream of 5'TSS. We denoted a loop as $L_i^g, i \in \{1, 2, \cdots, N\}$ where N is the total number of P-D loops in a gene g. We further defined the loop intensity (LI) of a gene as $LI_g = sum(L_i^g)$. For the gene with at least one loop, we considered it as a looping gene (denoted as LG).

There are four stepwise process to identify four levels of looping genes. The first level is to identify individual TT-specific differential looping genes, $IDLG_{\text{Ts.vs.NTs}}$, identified by comparing each individual TT to NTs. We denoted gained looing genes as GLG and lost looping genes as LLG. The second level is to identify individual RT-specific differential looping genes, $IDLG_{RTs.vs.PTs}$. The third level is to identify common TR cell-specific differential looping genes with individual RT-specific differential looping genes, $DLG_{nRTs.vsPTs}^{TR}$, defined as the common looping genes between $IDLG_{Ts.vs.NTs}$ and TR-specific differential looping genes. The fourth level is to identify differentially expressed looping genes, $DELG_{nRTs.vsPTs}^{TR}$, obtained by intersecting TR-specific DEGs with $DLG_{nRTs.vsPTs}^{TR}$. The detailed analyses were described as the following:

1. Normalizing loop intensity (LI) with a median of ratio method to remove the Hi-C library size bias. We first constructed a loop intensity matrix (M_{LI}), in which each column represents a tissue sample and each row represents a looping gene. The elements in M_{LI} were the $Ll_g^s, s \in \{samples\}$ and we applied geometric average function to each row of M_{LI}. All looping genes with an infinity geometric average value were filtered out and the resulting matrix was denoted as M_{LI}^{filt}. We further subtracted geometric average values of looping genes from M_{LI}^{filt} to form $M_{LI}^{filt\_sub}$ and calculated the column-based medians of $M_{LI}^{filt\_sub}$. Next, we made an exponential of the medians as the normalizing factors $coef_n$ for each tissue sample. Lastly, we divided the original M_{LI} by the $coef_n$, and got the final normalized matrix mM_{LI}^{nor}.

2. Identifying $IDLG_{TTs.vs.NTs}$. We first applied a Z-score function to each row of M_{LI}^{norm}; Then, we calculated signed Euclidean distance of looping genes (denoted as D_g^{TT}) between individual tumor tissue and normal tissues:

$$signD_g^{TT} = Sign\left(\overline{LI_g^{TTs}} \geq \overline{LI_g^{NTs}}\right) \times Eucdist\left(LI_g^{TT}, LI_g^{NTs}\right) \quad \text{(Equation 10)}$$

Where Sign is a sign function, $TT \in TTs = \{PT1, \cdots, PT5, RT1, \cdots RT5\}$ and $NTs = \{NT1, NT2\}$. Next, we fitted the probability density function (PDF) of D_g^{TT} with the bi-gaussian model:

$$PDF_{D_g^{TT}} = A_1 e^{-\frac{(x-\mu_1)^2}{2\sigma_1^2}} + A_2 e^{-\frac{(x-\mu_2)^2}{2\sigma_2^2}} \quad \text{(Equation 11)}$$

where (A_1, A_2, μ_1, μ_2, σ_1, σ_2) are gaussian parameters that learned from the $D_g^{TT's}$ distribution; Finally, we calculated D value at half maximum height (HMH) of PDFs as the cutoff and identified the individual TT-specific looping genes by H$abs\left(D_g^{TT}\right) \geq D_{HM}$;

3. Identifying $IDLG_{RTs.vs.PTs}$. We first retrieved looping genes occurred in at least two PTs ($CIDLG_{PTs.vs.NTs}$). Then, we built a binary matrix by outer-joining $CIDLG_{PTs.vs.NTs}$ and $IDLG_{RTs.vs.NTs}$ as rows and $\{RT1, \cdots RT5, PT_c\}$ as columns. 0 and 1 in the matrix represent the looping genes absent and existence, respectively. Finally, we subtracted PT_c column from each RT column and thus identified $IDLG_{RTs.vs.PTs}$ when the subtracted result equal to 1.

4. Identifying $DLG_{nRTs.vsPTs}^{TR}$. We first identified TR-specific differential looping genes, DLG^{TR}, by comparing TR and TTS cell lines with the method described above. We then defined several classes of common individual RT-specific differential looping genes, denote as $DLG_{nRTs.vs.PTs}$: $D\ LG_{1RTs.vs.PTs}$ (genes shared in at least one RTs), $DLG_{2RTs.vs.PTs}$ (genes shared in at least two RTs), up to $DLG_{5RTs.vs.PTs}$ (genes shared in all five RTs). Lastly, we identified $DLG_{nRTs.vsPTs}^{TR}$ as the overlapped DLGs between $D\ LG^{TR}$ and s$D\ LG_{nRTs.vs.PT}$.

5. Identifying $DELG_{nRTs.vsPTs}^{TR}$. We processed DEGs in TR cell lines denoted as DEG^{TR}, as described in Li .et al[43] and we intersected $DLG_{nRTs.vsPTs}^{TR}$ and DEG^{TR} to obtain $DELG_{nRTs.vsPTs}^{TR}$. The visualization of looping genes was performed by pygenomtracks[67]

CNV analysis: We applied HiNT-CNV, a module within HiNT[27] to identify CNVs from the contact matrix generated by HiC-Pro. The algorithm of CNV detection in HiNT tool utilizes a regression-based method to remove known biases and a minimizing Bayesian information criterion (BIC) procedure to get the final CNV profile. HiNT-CNV is able to take the contact matrix as the input as well as take FASTQ/BAM as the input. It outputs statistically significant CNVs. We used the default parameters in our analysis.

Gene ontologies (GO), pathways and survival analyses: We performed the GO, pathways and survival analyses as previous described.[43] We applied DAVID[29,86] and Enrichr[30] to perform the pathway analysis on $LG_{2RTs.vs.PTs}$. We also used an online survival tool (www.kmplot.com)[31] to analyze the prognostic value of genes on breast cancer prognosis using microarray data of 1,809 patients in terms of relapse free survival, overall survival, and distant metastasis free survival. A survival curve was displayed with the hazard ratio with 95% confidence intervals and a logrank P value.

QUANTIFICATION AND STATISTICAL ANALYSIS

No statistical methods were used to predetermine sample sizes, but the sample sizes here are similar to those reported in previous publications. No randomization was used during data collection as there was a single experimental condition for all acquired data. Data collection and analyses were not performed blind to the conditions of the experiments as all experiments followed the same experimental condition. Statistical details of experiments and analyses can be found in the figure legends and main text above. All statistical tests were two-sided, and statistical significance was considered when P value < 0.05. To account for multiple testing, the P values were adjusted using the bonferroni correction.

Supplementary Material

Refer to Web version on PubMed Central for supplementary material.

ACKNOWLEDGMENTS

We thank the UTHSA Next Generation Sequencing Facilities and Dr. Zhao Lai for sequencing Hi-C data. This project was partially supported by grants from the NIH R01GM114142 and an Advancing a Healthier Wisconsin (AHW) Seed Grant.

REFERENCES

1. Miller WR, Bartlett JMS, Canney P, and Verrill M (2007). Hormonal therapy for postmenopausal breast cancer: the science of sequencing. Breast Cancer Res. Treat. 103, 149–160. [PubMed: 17039263]
2. Brodie A, and Sabnis G (2011). Adaptive changes result in activation of alternate signaling pathways and acquisition of resistance to aromatase inhibitors. Clin. Cancer Res. 17, 4208–4213. [PubMed: 21415222]
3. Ring A, and Dowsett M (2004). Mechanisms of tamoxifen resistance. Endocr. Relat. Cancer 11, 643–658. [PubMed: 15613444]
4. Pinder SE, Ellis IO, and Elston CW (1995). Prognostic factors in primary breast carcinoma. J. Clin. Pathol. 48, 981–983. [PubMed: 8543641]
5. Elston CW, Ellis IO, and Pinder SE (1999). Pathological prognostic factors in breast cancer. Crit. Rev. Oncol. Hematol. 31, 209–223. [PubMed: 10532196]

6. Perou CM, Sørlie T, Eisen MB, Van De Rijn M, Jeffrey SS, Rees CA, Pollack JR, Ross DT, Johnsen H, Akslen LA, et al. (2000). Molecular portraits of human breast tumours. nature 406, 747–752. [PubMed: 10963602]
7. Chanrion M, Negre V, Fontaine H, Salvetat N, Bibeau F, Mac Grogan G, Mauriac L, Katsaros D, Molina F, Theillet C, and Darbon JM (2008). A gene expression signature that can predict the recurrence of tamoxifen-treated primary breast cancer. Clin. Cancer Res. 14, 1744–1752. [PubMed: 18347175]
8. Cancer Genome Atlas Network (2012). Comprehensive molecular portraits of human breast tumours. Nature 490, 61–70. [PubMed: 23000897]
9. Ciriello G, Gatza ML, Beck AH, Wilkerson MD, Rhie SK, Pastore A, Zhang H, McLellan M, Yau C, Kandoth C, et al. (2015). Comprehensive molecular portraits of invasive lobular breast cancer. Cell 163, 506–519. [PubMed: 26451490]
10. Rueda OM, Sammut S-J, Seoane JA, Chin S-F, Caswell-Jin JL, Callari M, Batra R, Pereira B, Bruna A, Ali HR, et al. (2019). Dynamics of breast-cancer relapse reveal late-recurring ER-positive genomic subgroups. Nature 567, 399–404. [PubMed: 30867590]
11. Lieberman-Aiden E, Van Berkum NL, Williams L, Imakaev M, Ragoczy T, Telling A, Amit I, Lajoie BR, Sabo PJ, Dorschner MO, et al. (2009). Comprehensive mapping of long-range interactions reveals folding principles of the human genome. science 326, 289–293. [PubMed: 19815776]
12. Dixon JR, Selvaraj S, Yue F, Kim A, Li Y, Shen Y, Hu M, Liu JS, and Ren B (2012). Topological domains in mammalian genomes identified by analysis of chromatin interactions. Nature 485, 376–380. [PubMed: 22495300]
13. Rao SSP, Huntley MH, Durand NC, Stamenova EK, Bochkov ID, Robinson JT, Sanborn AL, Machol I, Omer AD, Lander ES, and Aiden EL (2014). A 3D map of the human genome at kilobase resolution reveals principles of chromatin looping. Cell 159, 1665–1680. [PubMed: 25497547]
14. Rhie SK, Perez AA, Lay FD, Schreiner S, Shi J, Polin J, and Farnham PJ (2019). A high-resolution 3D epigenomic map reveals insights into the creation of the prostate cancer transcriptome. Nat. Commun. 10, 4154. [PubMed: 31515496]
15. Zhou Y, Gerrard DL, Wang J, Li T, Yang Y, Fritz AJ, Rajendran M, Fu X, Stein G, Schiff R, et al. (2019). Temporal dynamic reorganization of 3D chromatin architecture in hormone-induced breast cancer and endocrine resistance. Nat. Commun. 10, 1522. [PubMed: 30944316]
16. Wu P, Li T, Li R, Jia L, Zhu P, Liu Y, Chen Q, Tang D, Yu Y, and Li C (2017). 3D genome of multiple myeloma reveals spatial genome disorganization associated with copy number variations. Nat. Commun. 8, 1937. [PubMed: 29203764]
17. Xu J, Song F, Lyu H, Kobayashi M, Zhang B, Zhao Z, Hou Y, Wang X, Luan Y, Jia B, et al. (2022). Subtype-specific 3D genome alteration in acute myeloid leukaemia. Nature 611, 387–398. [PubMed: 36289338]
18. Johnstone SE, Reyes A, Qi Y, Adriaens C, Hegazi E, Pelka K, Chen JH, Zou LS, Drier Y, Hecht V, et al. (2020). Large-scale topological changes restrain malignant progression in colorectal cancer. Cell 182, 1474–1489.e23. [PubMed: 32841603]
19. Kloetgen A, Thandapani P, Ntziachristos P, Ghebrechristos Y, Nomikou S, Lazaris C, Chen X, Hu H, Bakogianni S, Wang J, et al. (2020). Three-dimensional chromatin landscapes in T cell acute lymphoblastic leukemia. Nat. Genet. 52, 388–400. [PubMed: 32203470]
20. Iyyanki T, Zhang B, Wang Q, Hou Y, Jin Q, Xu J, Yang H, Liu T, Wang X, Song F, et al. (2021). Subtype-associated epigenomic landscape and 3D genome structure in bladder cancer. Genome Biol. 22, 105–120. [PubMed: 33858483]
21. Ebert P, Audano PA, Zhu Q, Rodriguez-Martin B, Porubsky D, Bonder MJ, Sulovari A, Ebler J, Zhou W, Serra Mari R, et al. (2021). Haplotype-resolved diverse human genomes and integrated analysis of structural variation. Science 372, eabf7117. [PubMed: 33632895]
22. Servant N, Varoquaux N, Lajoie BR, Viara E, Chen C-J, Vert J-P, Heard E, Dekker J, and Barillot E (2015). HiC-Pro: an optimized and flexible pipeline for Hi-C data processing. Genome Biol. 16, 259–311. [PubMed: 26619908]

23. Chakraborty A, Wang JG, and Ay F (2022). dcHiC detects differential compartments across multiple Hi-C datasets. Nat. Commun. 13, 6827. [PubMed: 36369226]
24. Shin H, Shi Y, Dai C, Tjong H, Gong K, Alber F, and Zhou XJ (2016). TopDom: an efficient and deterministic method for identifying topological domains in genomes. Nucleic Acids Res. 44, e70. [PubMed: 26704975]
25. Misteli T (2020). The self-organizing genome: principles of genome architecture and function. Cell 183, 28–45. [PubMed: 32976797]
26. Kaul A, Bhattacharyya S, and Ay F (2020). Identifying statistically significant chromatin contacts from Hi-C data with FitHiC2. Nat. Protoc. 15, 991–1012. [PubMed: 31980751]
27. Wang S, Lee S, Chu C, Jain D, Kerpedjiev P, Nelson GM, Walsh JM, Alver BH, and Park PJ (2020). HiNT: a computational method for detecting copy number variations and translocations from Hi-C data. Genome Biol. 21, 1–15.
28. Yang Y, Choppavarapu L, Fang K, Naeini AS, Nosirov B, Li J, Yang K, He Z, Zhou Y, Schiff R, et al. (2020). The 3D genomic landscape of differential response to EGFR/HER2 inhibition in endocrine-resistant breast cancer cells. Biochim. Biophys. Acta. Gene Regul. Mech. 1863, 194631. [PubMed: 32956836]
29. Huang DW, Sherman BT, Tan Q, Kir J, Liu D, Bryant D, Guo Y, Stephens R, Baseler MW, Lane HC, and Lempicki RA (2007). DAVID Bioinformatics Resources: expanded annotation database and novel algorithms to better extract biology from large gene lists. Nucleic Acids Res. 35, W169–W175. [PubMed: 17576678]
30. Kuleshov MV, Jones MR, Rouillard AD, Fernandez NF, Duan Q, Wang Z, Koplev S, Jenkins SL, Jagodnik KM, Lachmann A, et al. (2016). Enrichr: a comprehensive gene set enrichment analysis web server 2016 update. Nucleic Acids Res. 44, W90–W97. [PubMed: 27141961]
31. Győrffy B (2021). Survival analysis across the entire transcriptome identifies biomarkers with the highest prognostic power in breast cancer. Comput. Struct. Biotechnol. J. 19, 4101–4109. [PubMed: 34527184]
32. Zhou R, Huang W, Yao Y, Wang Y, Li Z, Shao B, Zhong J, Tang M, Liang S, Zhao X, et al. (2013). CA II, a potential biomarker by proteomic analysis, exerts significant inhibitory effect on the growth of colorectal cancer cells. Int. J. Oncol. 43, 611–621. [PubMed: 23727877]
33. Waterman EA, Cross NA, Lippitt JM, Cross SS, Rehman I, Holen I, Hamdy FC, and Eaton CL (2007). The antibody MAB8051 directed against osteoprotegerin detects carbonic anhydrase II: Implications for association studies with human cancers. Int. J. Cancer 121, 1958–1966. [PubMed: 17631639]
34. Liu CM, Lin YM, Yeh KT, Chen MK, Chang JH, Chen CJ, Chou MY, Yang SF, and Chien MH (2012). Expression of carbonic anhydrases I/II and the correlation to clinical aspects of oral squamous cell carcinoma analyzed using tissue microarray. J. Oral Pathol. Med. 41, 533–539. [PubMed: 22416960]
35. Liu L-C, Xu W-T, Wu X, Zhao P, Lv Y-L, and Chen L (2013). Overexpression of carbonic anhydrase II and Ki-67 proteins in prognosis of gastrointestinal stromal tumors. World J. Gastroenterol. 19, 2473–2480. [PubMed: 23674848]
36. Faubert B, Solmonson A, and DeBerardinis RJ (2020). Metabolic reprogramming and cancer progression. Science 368, eaaw5473. [PubMed: 32273439]
37. Zhao K, Schäfer A, Zhang Z, Elsässer K, Culmsee C, Zhong L, Pagenstecher A, Nimsky C, and Bartsch JW (2021). Inhibition of carbonic anhydrase 2 overcomes temozolomide resistance in glioblastoma cells. Int. J. Mol. Sci. 23, 157. [PubMed: 35008590]
38. Rathod KR, and Ganatra TH (2018). Evaluation of anti-cancer activity of Brinzolamide with special emphasis on blood cancer (Polycethemia Rubra Vera) in vivo. Int. J. Pharmtech Res. 11, 177–189.
39. Chakraborty A, and Ay F (2019). The Role of 3D Genome Organization in Disease: From Compartments to Single Nucleotides (Elsevier), pp. 104–113.
40. Zheng H, and Xie W (2019). The role of 3D genome organization in development and cell differentiation. Nat. Rev. Mol. Cell Biol. 20, 535–550. [PubMed: 31197269]
41. Barutcu AR, Lajoie BR, McCord RP, Tye CE, Hong D, Messier TL, Browne G, van Wijnen AJ, Lian JB, Stein JL, et al. (2015). Chromatin interaction analysis reveals changes in small

chromosome and telomere clustering between epithelial and breast cancer cells. Genome Biol. 16, 1–14. [PubMed: 25583448]

42. Achinger-Kawecka J, Valdes-Mora F, Luu P-L, Giles KA, Caldon CE, Qu W, Nair S, Soto S, Locke WJ, Yeo-Teh NS, et al. (2020). Epigenetic reprogramming at estrogen-receptor binding sites alters 3D chromatin landscape in endocrine-resistant breast cancer. Nat. Commun. 11, 320. [PubMed: 31949157]
43. Li J, Fang K, Choppavarapu L, Yang K, Yang Y, Wang J, Cao R, Jatoi I, and Jin VX (2021). Hi-C profiling of cancer spheroids identifies 3D-growth-specific chromatin interactions in breast cancer endocrine resistance. Clin. Epigenetics 13, 175–213. [PubMed: 34535185]
44. Kyriazoglou A, Liontos M, Zakopoulou R, Kaparelou M, Tsiara A, Papatheodoridi AM, Georgakopoulou R, and Zagouri F (2021). The role of the Hippo pathway in breast cancer carcinogenesis, prognosis, and treatment: a systematic review. Breast Care 16, 6–15. [PubMed: 33716627]
45. Finlay-Schultz J, and Sartorius CA (2015). Steroid hormones, steroid receptors, and breast cancer stem cells. J. Mammary Gland Biol. Neoplasia 20, 39–50. [PubMed: 26265122]
46. Hanahan D (2022). Hallmarks of cancer: new dimensions. Cancer Discov. 12, 31–46. [PubMed: 35022204]
47. Fang K, Ohihoin AG, Liu T, Choppavarapu L, Nosirov B, Wang Q, Yu X-Z, Kamaraju S, Leone G, and Jin VX (2024). Integrated single-cell analysis reveals distinct epigenetic-regulated cancer cell states and a heterogeneity-guided core signature in tamoxifen-resistant breast cancer. Genome Med. 16, 134. [PubMed: 39558215]
48. Jögi A, Ehinger A, Hartman L, and Alkner S (2019). Expression of HIF-1α is related to a poor prognosis and tamoxifen resistance in contralateral breast cancer. PLoS One 14, e0226150. [PubMed: 31821370]
49. Loh YN, Hedditch EL, Baker LA, Jary E, Ward RL, and Ford CE (2013). The Wnt signalling pathway is upregulated in an in vitro model of acquired tamoxifen resistant breast cancer. BMC Cancer 13, 174–179. [PubMed: 23547709]
50. Stone JK, Kim J-H, Vukadin L, Richard A, Giannini HK, Lim S-TS, Tan M, and Ahn E-YE (2019). Hypoxia induces cancer cell-specific chromatin interactions and increases MALAT1 expression in breast cancer cells. J. Biol. Chem. 294, 11213–11224. [PubMed: 31167784]
51. Kim T, Han S, Chun Y, Yang H, Min H, Jeon SY, Kim J. i., Moon H-G, and Lee D (2022). Comparative characterization of 3D chromatin organization in triple-negative breast cancers. Exp. Mol. Med. 54, 585–600. [PubMed: 35513575]
52. Fudenberg G, Imakaev M, Lu C, Goloborodko A, Abdennur N, and Mirny LA (2016). Formation of chromosomal domains by loop extrusion. Cell Rep. 15, 2038–2049. [PubMed: 27210764]
53. Sanborn AL, Rao SSP, Huang S-C, Durand NC, Huntley MH, Jewett AI, Bochkov ID, Chinnappan D, Cutkosky A, Li J, et al. (2015). Chromatin extrusion explains key features of loop and domain formation in wild-type and engineered genomes. Proc. Natl. Acad. Sci. USA 112, E6456–E6465. [PubMed: 26499245]
54. Alipour E, and Marko JF (2012). Self-organization of domain structures by DNA-loop-extruding enzymes. Nucleic Acids Res. 40, 11202–11212. [PubMed: 23074191]
55. Hansen AS, Cattoglio C, Darzacq X, and Tjian R (2018). Recent evidence that TADs and chromatin loops are dynamic structures. Nucleus 9, 20–32. [PubMed: 29077530]
56. Wang X, Yan J, Ye Z, Zhang Z, Wang S, Hao S, Shen B, and Wei G (2022). Reorganization of 3D chromatin architecture in doxorubicin-resistant breast cancer cells. Front. Cell Dev. Biol. 10, 974750. [PubMed: 36003143]
57. Mboge MY, Mahon BP, McKenna R, and Frost SC (2018). Carbonic anhydrases: role in pH control and cancer. Metabolites 8, 19. [PubMed: 29495652]
58. Lee S, Toft NJ, Axelsen TV, Espejo MS, Pedersen TM, Mele M, Pedersen HL, Balling E, Johansen T, Burton M, et al. (2023). Carbonic anhydrases reduce the acidity of the tumor microenvironment, promote immune infiltration, decelerate tumor growth, and improve survival in ErbB2/HER2-enriched breast cancer. Breast Cancer Res. 25, 46. [PubMed: 37098526]
59. DeSantis L (2000). Preclinical overview of brinzolamide. Surv. Ophthalmol. 44, S119–S129. [PubMed: 10665514]

60. Supuran CT (2008). Carbonic anhydrases: novel therapeutic applications for inhibitors and activators. Nat. Rev. Drug Discov. 7, 168–181. [PubMed: 18167490]
61. Pinard MA, Boone CD, Rife BD, Supuran CT, and McKenna R (2013). Structural study of interaction between brinzolamide and dorzolamide inhibition of human carbonic anhydrases. Bioorg. Med. Chem. 21, 7210–7215. [PubMed: 24090602]
62. Leu Y-W, Yan PS, Fan M, Jin VX, Liu JC, Curran EM, Welshons WV, Wei SH, Davuluri RV, Plass C, et al. (2004). Loss of estrogen receptor signaling triggers epigenetic silencing of downstream targets in breast cancer. Cancer Res. 64, 8184–8192. [PubMed: 15548683]
63. Morley P, Whitfield JF, Vanderhyden BC, Tsang BK, and Schwartz J-L (1992). A new, nongenomic estrogen action: the rapid release of intracellular calcium. Endocrinology 131, 1305–1312. [PubMed: 1505465]
64. Bi M, Zhang Z, Jiang Y-Z, Xue P, Wang H, Lai Z, Fu X, De Angelis C, Gong Y, Gao Z, et al. (2020). Enhancer reprogramming driven by high-order assemblies of transcription factors promotes phenotypic plasticity and breast cancer endocrine resistance. Nat. Cell Biol. 22, 701–715. [PubMed: 32424275]
65. Tareen A, and Kinney JB (2020). Logomaker: beautiful sequence logos in Python. Bioinformatics 36, 2272–2274. [PubMed: 31821414]
66. van der Weide RH, van den Brand T, Haarhuis JHI, Teunissen H, Rowland BD, and de Wit E (2021). Hi-C analyses with GENOVA: a case study with cohesin variants. NAR Genom. Bioinform. 3, lqab040. [PubMed: 34046591]
67. Lopez-Delisle L, Rabbani L, Wolff J, Bhardwaj V, Backofen R, Grüning B, Ramírez F, and Manke T (2021). pyGenomeTracks: reproducible plots for multivariate genomic datasets. Bioinformatics 37, 422–423. [PubMed: 32745185]
68. Quinlan AR, and Hall IM (2010). BEDTools: a flexible suite of utilities for comparing genomic features. Bioinformatics 26, 841–842. [PubMed: 20110278]
69. Dennis G Jr, Sherman BT, Hosack DA, Yang J, Gao W, Lane HC, and Lempicki RA (2003). DAVID: Database for Annotation, Visualization, and Integrated Discovery. Genome Biol. 4, P3. [PubMed: 12734009]
70. Lánczky A, and Győrffy B (2021). Web-Based Survival Analysis Tool Tailored for Medical Research (KMplot): Development and Implementation. J. Med. Internet Res. 23.
71. Cresswell KG, and Dozmorov MG (2020). TADCompare: an R package for differential and temporal analysis of topologically associated domains. Front. Genet. 11, 158. [PubMed: 32211023]
72. Massarweh S, Osborne CK, Creighton CJ, Qin L, Tsimelzon A, Huang S, Weiss H, Rimawi M, and Schiff R (2008). Tamoxifen resistance in breast tumors is driven by growth factor receptor signaling with repression of classic estrogen receptor genomic function. Cancer Res. 68, 826–833. [PubMed: 18245484]
73. Morrison G, Fu X, Shea M, Nanda S, Giuliano M, Wang T, Klinowska T, Osborne CK, Rimawi MF, and Schiff R (2014). Therapeutic potential of the dual EGFR/HER2 inhibitor AZD8931 in circumventing endocrine resistance. Breast Cancer Res. Treat. 144, 263–272. [PubMed: 24554387]
74. Feng Q, Zhang Z, Shea MJ, Creighton CJ, Coarfa C, Hilsenbeck SG, Lanz R, He B, Wang L, Fu X, et al. (2014). An epigenomic approach to therapy for tamoxifen-resistant breast cancer. Cell Res. 24, 809–819. [PubMed: 24874954]
75. Osborne CK, Jarman M, McCague R, Coronado EB, Hilsenbeck SG, and Wakeling AE (1994). The importance of tamoxifen metabolism in tamoxifen-stimulated breast tumor growth. Cancer Chemother. Pharmacol. 34, 89–95. [PubMed: 8194171]
76. Hagege H, Klous P, Braem C, Splinter E, Dekker J, Cathala G, De Laat W, and Forné T (2007). Quantitative analysis of chromosome conformation capture assays (3C-qPCR). Nat. Protoc. 2, 1722–1733. [PubMed: 17641637]
77. Dekker J (2006). The three'C's of chromosome conformation capture: controls, controls, controls. Nat. Methods 3, 17–21. [PubMed: 16369547]

78. Zhou Y, He Z, Li T, Choppavarapu L, Hu X, Cao R, Leone GW, Kahn M, and Jin VX (2024). 3D Chromatin Alteration by Disrupting b-Catenin/CBP Interaction Is Enriched with Insulin Signaling in Pancreatic Cancer. Cancers 16, 2202. [PubMed: 38927910]

79. Lavanya C, Venkataswamy MM, Sibin MK, Srinivas Bharath MM, and Chetan GK (2018). Down regulation of human telomerase reverse transcriptase (hTERT) expression by BIBR1532 in human glioblastoma LN18 cells. Cytotechnology 70, 1143–1154. [PubMed: 29546682]

80. Lavanya C, Sibin MK, Srinivas Bharath MM, Manoj MJ, Venkataswamy MM, Bhat DI, Narasinga Rao KVL, and Chetan GK (2016). RNA interference mediated downregulation of human telomerase reverse transcriptase (hTERT) in LN18 cells. Cytotechnology 68, 2311–2321. [PubMed: 27757712]

81. Zufferey M, Tavernari D, Oricchio E, and Ciriello G (2018). Comparison of computational methods for the identification of topologically associating domains. Genome Biol. 19, 217–218. [PubMed: 30526631]

82. Sauerwald N, Singhal A, and Kingsford C (2020). Analysis of the structural variability of topologically associated domains as revealed by Hi-C. NAR Genom. Bioinform. 2, lqz008.

83. Chen F, Li G, Zhang MQ, and Chen Y (2018). HiCDB: a sensitive and robust method for detecting contact domain boundaries. Nucleic Acids Res. 46, 11239–11250. [PubMed: 30184171]

84. Nag S, Zhu X, Deng J, Song Y-Z, and Xiang T (2023). Difftad: Temporal Action Detection with Proposal Denoising Diffusion. arXiv, 10362–10374. 10.48550/arXiv.2303.14863.

85. Wang G, Meng Q, Xia B, Zhang S, Lv J, Zhao D, Li Y, Wang X, Zhang L, Cooke JP, et al. (2020). TADsplimer reveals splits and mergers of topologically associating domains for epigenetic regulation of transcription. Genome Biol. 21, 1–16.

86. Huang DW, Sherman BT, and Lempicki RA (2009). Systematic and integrative analysis of large gene lists using DAVID bioinformatics resources. Nat. Protoc. 4, 44–57. [PubMed: 19131956]

Highlights

- Highly heterogeneous TADs and intensively variable loops are observed among breast tumors
- A looping-mediated CA2 plays a role in driving tamoxifen resistance
- The inhibition of CA2 impedes tumor growth and reverses looping
- The disruption of CA2 looping reduces cancer cell proliferation and CA2 gene expression

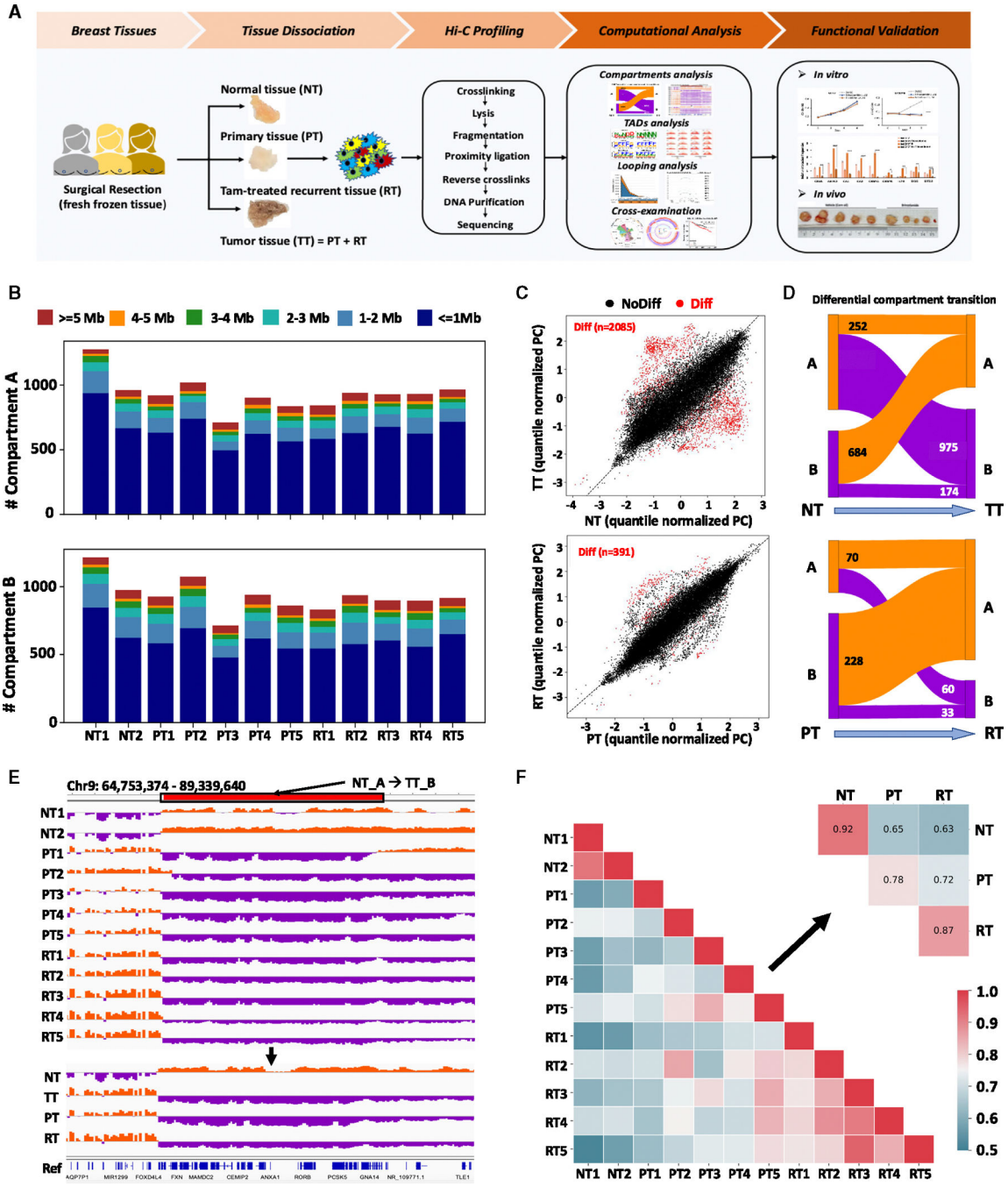

Figure 1. Compartments are largely preserved among breast tumors

(A) A workflow of the study. Twelve normal and tumor breast tissues were collected, including two NTs, five PTs, and five RTs. Hi-C profiling was then performed for each tissue and generated ~3 billion reads. Computational analyses were further conducted to investigate the three layers of genome organization, including compartment, TADs, and chromatin loops, and *in silico* analyses were performed to identify enriched biological pathways and to predict clinical outcome. *In vitro* and *in vivo* functional characterization was performed to elicit the looping-mediated biological pathway.

(B) Stacked bar plots showing the numbers of compartments A and B in different lengths in each of 12 normal and tumor tissues. The number of compartments was around 2,000 across tissues, and the length of the majority of compartments A and B was less than 1 Mb.
(C) Scatterplots displaying the number of 100-kb bins with statistically differential compartmentalization identified by dcHiC. The number of differential compartments between TT and NT was 2,085, and the number between PT and RT was 391. NT, NT1–2; PT, PT1–5; RT, RT1–5.
(D) Sankey plots illustrating the breakdown of the numbers of differential compartment calls (100-kb resolution) belonging to different types, including flipping (A to B, B to A) and matching (A to A and B to B). Compartment A is in dark orange, and compartment B is in dark violet.
(E) An IGV screenshot showing compartment A in NTs' transition to compartment B in TTs.
(F) The lower triangle heatmap demonstrates the Pearson correlation of compartmentalization between each two tissue samples, and the upper triangle heatmap shows the group-level Pearson correlation within (intra)/between (inter) NT, PT, and RT groups. Generally, the intragroup correlation is higher than the intergroup correlation. For intergroup correlations, the RT-PT correlation is higher than the PT-NT and RT-NT groups.

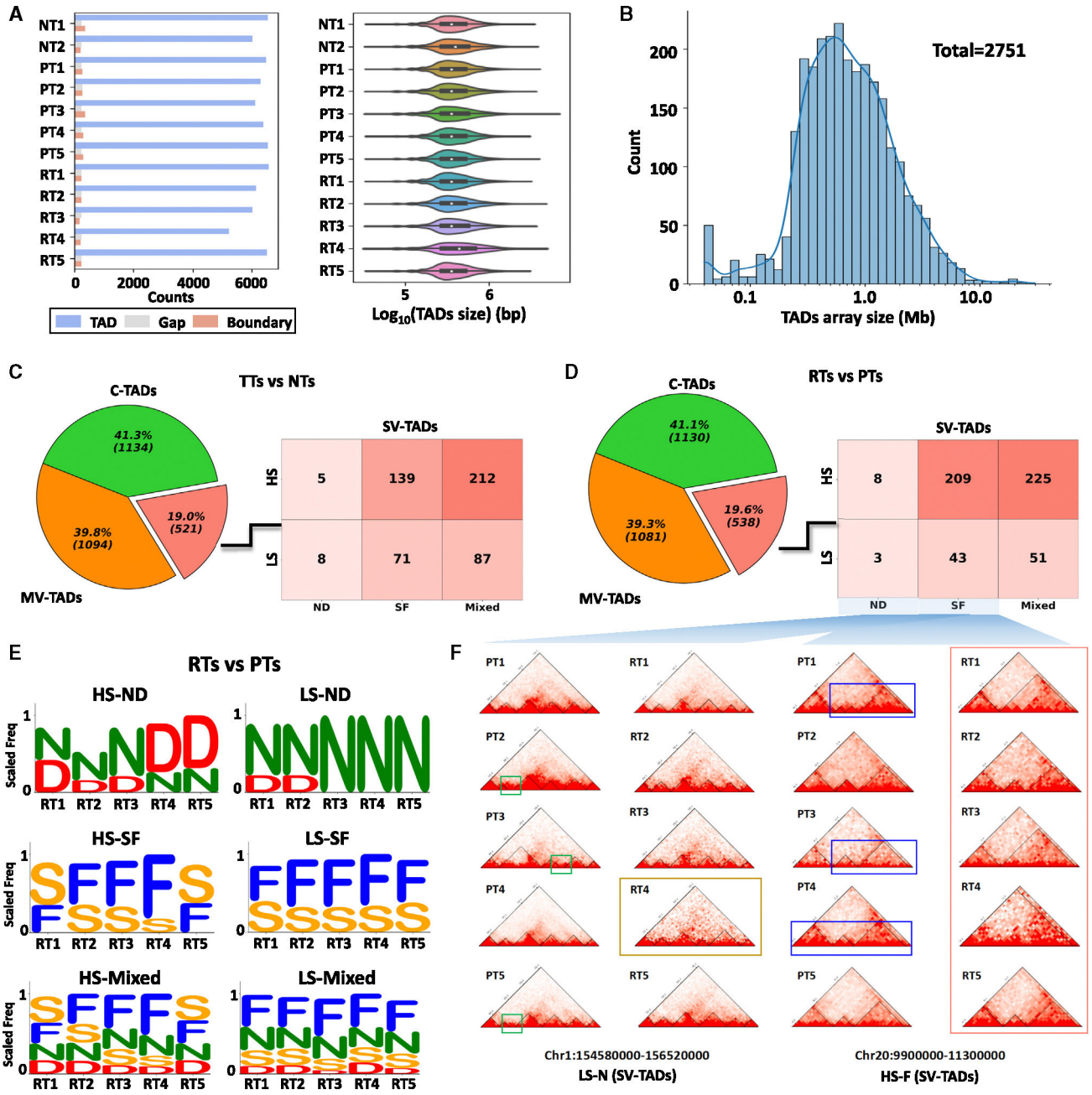

Figure 2. TADs are highly heterogeneous among breast tumors

(A) Bar plot (left) showing the numbers of TADs, gaps, and boundaries identified in the tissues. Violin plot (right) showing the distribution of TAD size.

(B) Histogram displaying the distribution of the size of the TAD array. The total number in the TAD array is 2,751.

(C) The pie chart on the left illustrates the proportions of the three comparison types, intertumor conserved TADs (C-TADs), intertumor moderately variable TADs (MV-TADs), and intertumor significantly variable TADs (SV-TADs), between TTs and NTs. The heatmap on the right demonstrates the numbers of six sub-categories within SV-TADs, composed of HS-ND, HS-SF, HS-mixed, LS-ND, LS-SF, and LS-mixed (STAR Methods).

(D) The pie chart on the left illustrates the proportions of the three types of TAD change between RT and PT. The heatmap on the right demonstrates the numbers of six sub-types, HS-ND, HS-SF, HS-mixed, LS-ND, LS-SF, and LS-mixed, within the SV-TADs of RT vs. PT.

(E) Logo plots showing the scaled frequency of four basic TAD change types, N(eo), D(eletion), S(plit), and F(use), for individual RTs by comparing RT vs. PT in six sub-categories. Top: the frequency of N/D/S/F in HS-ND and LS-ND. Middle: the frequency of N/D/S/F in HS-SF and LS-SF. Bottom: the frequency of N/D/S/F in HS-mixed and LS-mixed.

(F) The visualization of LS-N and HS-F within RT vs. PT. The green frame indicates ND and SF change, the brown frame indicates IMC (only RT4 differs; RT1, RT2, RT3, and RT5 are similar), the blue frame indicates those TADs fused in RTs (Fused -TADs in RTs), and the pink frame on the left point indicates LS (only RT4 has a different TAD array compared with other RTs) and on the right points indicates HS (five RTs have three different TAD arrays).

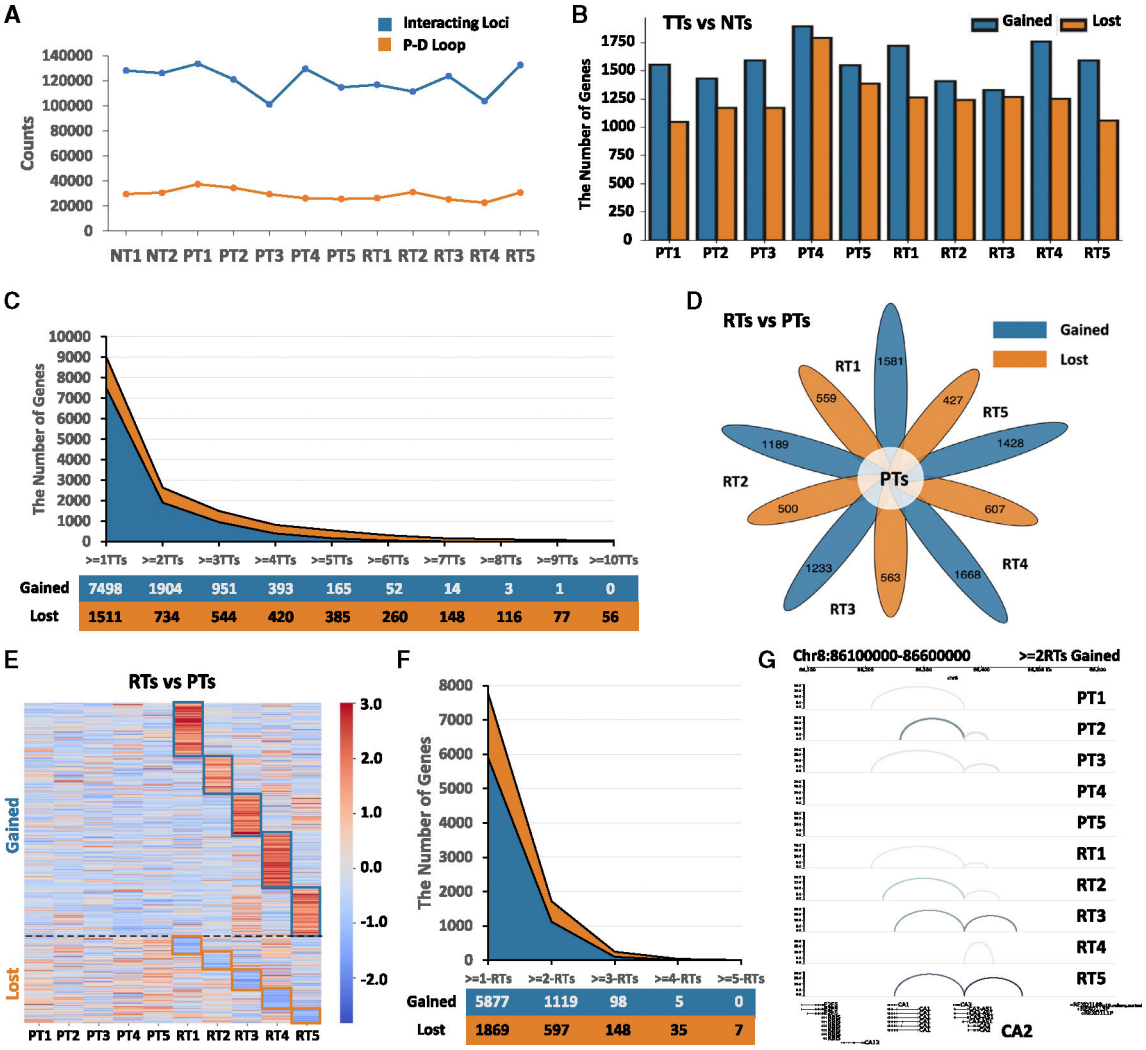

Figure 3. Chromatin loops are intensively variable among breast tumors

(A) Line plot showing the number of interacting loci and P-D loops (promoter-distal loops for a same gene) of each tissue.

(B) Bar plot illustrating the number of individual tumor-specific looping genes.

(C) Stacked line plot showing the number of common DLGs among the 10 TTs.

(D) Flower plot showing the number of individual RT-specific looping genes compared to PTs.

(E) Heatmap illustrating the loop intensity of individual RT-specific DLGs.

(F) Stacked line plot showing the number of common DLGs among the five RTs.

(G) Genome tracks displaying the CA2 DL loops belonging to ≥2RT GLGs. The color bar represents the intensity of loops ranging from 0 to 20. The darker the color, the higher the intensity of loops.

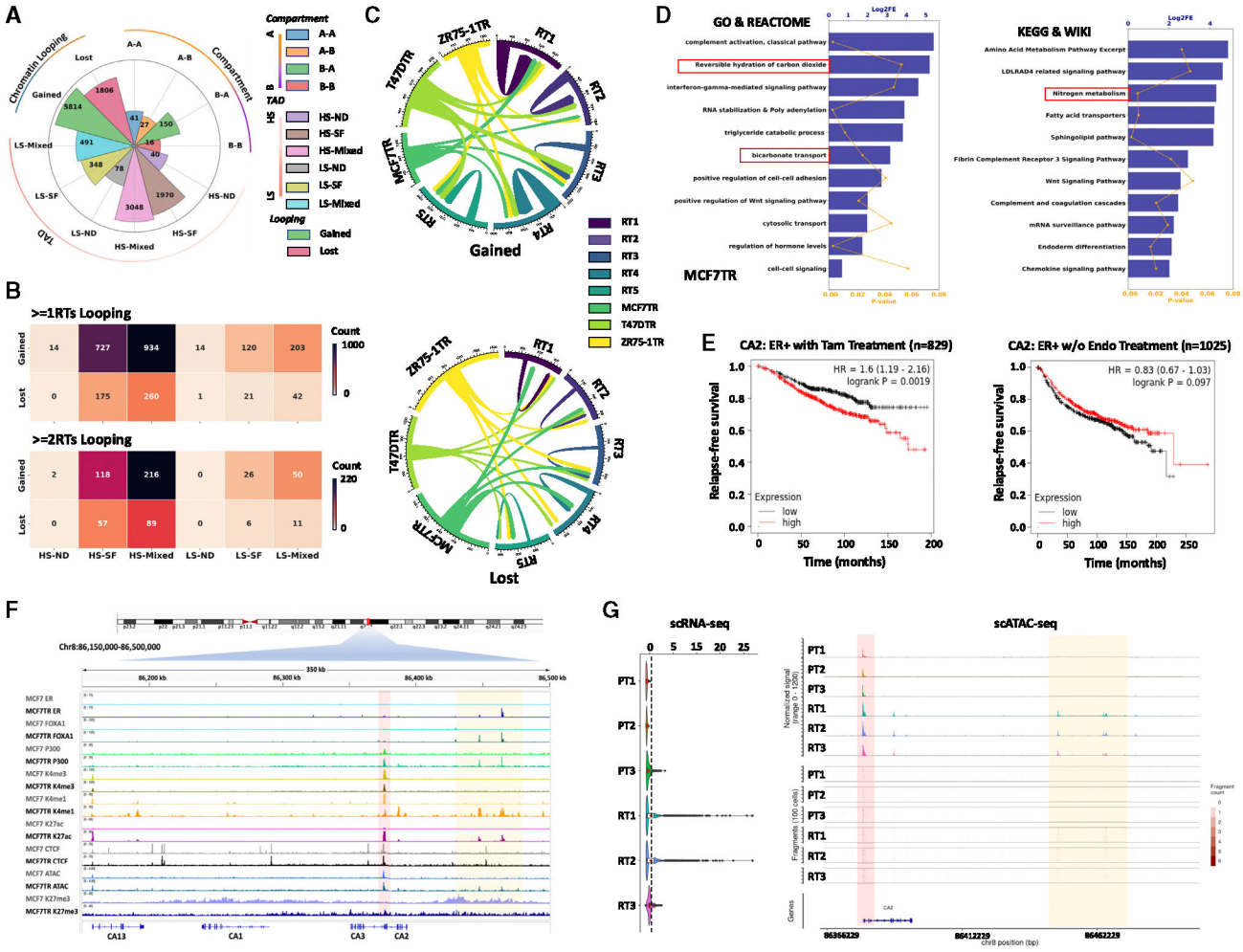

Figure 4. Cross-examination identifies RT-specific looping-mediated biological pathways

(A) Circle bar plot showing the number of common genes among the changes of three layers of chromatin architecture.

(B) Heatmaps showing the numbers of common genes between six types of TAD change and two types of looping change. The top is for at least one IDLG (individual differential looping gene), while the bottom is for at least two IDLGs.

(C) The top chord diagram shows the GLGs overlapping between three TR cell lines (MCF7TR, T47DTR, and ZR75–1TR) and five RTs, and the bottom chord diagram shows the LLGs overlapping between three TR cell lines and five RTs.

(D) Bar plots showing the top enriched terms of GO, REACTOME, KEGG, and WIKI for ≥2RTs_MCF7TR DELGs. The pathways within the red boxes are composed of CA1 and CA2.

(E) Kaplan-Meier plots of CA2 showing the probability of relapse-free survival in ER+ breast cancer patients with tamoxifen treatment (n = 829) and without endocrine treatment (n = 1,025). CA2 gene expression was classified as low or high (black or red lines, respectively) based on the comparison of its median cutoff value. The p value was determined by the log rank test.

(F) IGV visualization of the enrichment of ER, FOXA1, P300, CTCF, H3K4me3, H3K4me1, H3K27ac, H3K27me3, and ATAC on the promoter and enhancer regions of CA2.

(G) Violin plot showing that the expression level of CA2 was higher in three RTs than in three PTs from scRNA-seq data (left). Red points indicate the mean of the expression level. The track from scATAC-seq (single-cell sequencing assay for transposase-accessible chromatin sequencing) data suggests that CA2 gained open chromatin signals at its promoter and enhancer regions (right). Note: scRNA-seq and scATAC-seq were conducted in a separate cohort of breast tumor tissues for an ongoing study.

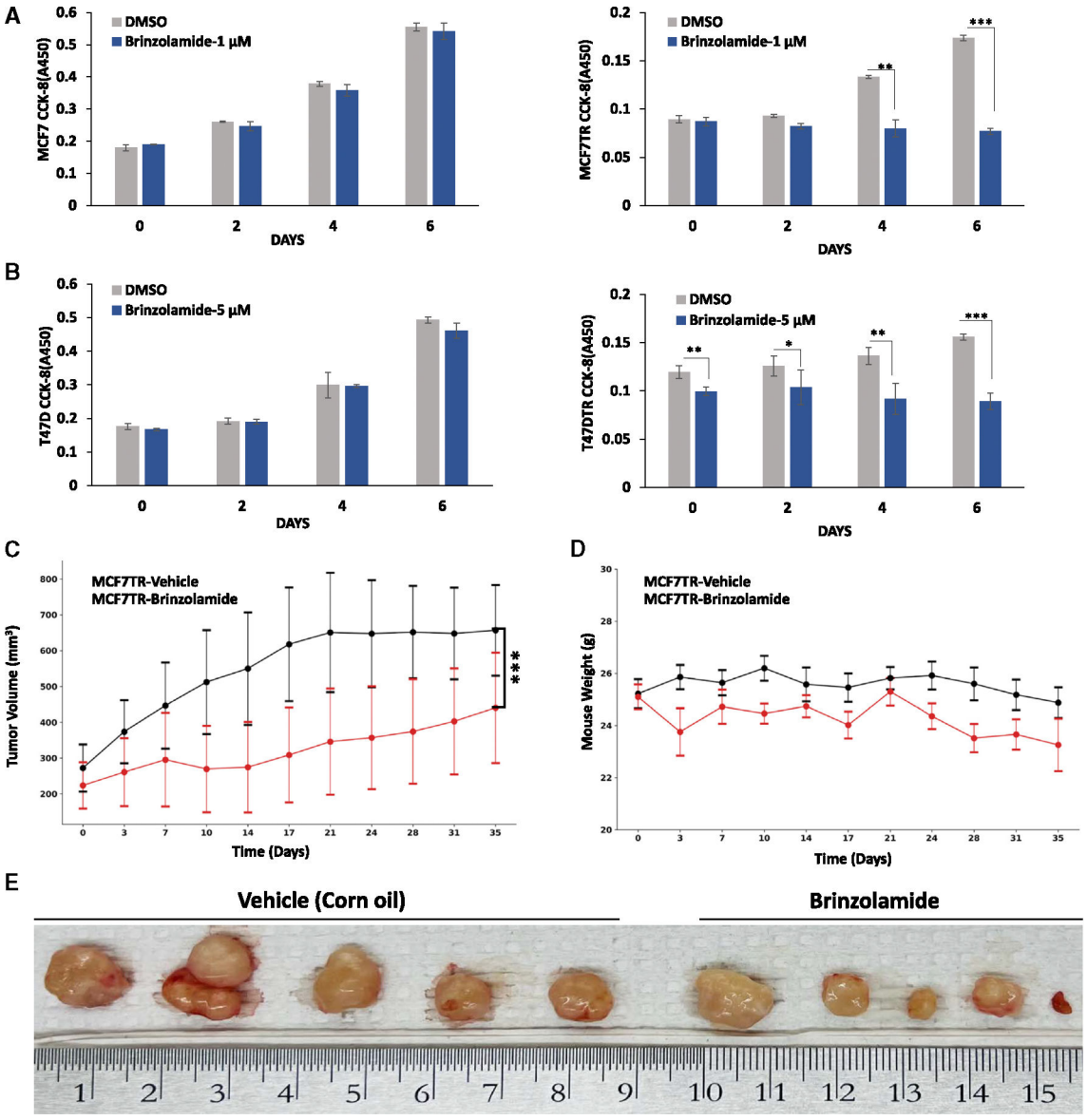

Figure 5. The inhibition of CA2 impedes tumor growth both *in vitro* and *in vivo*

(A) CCK-8 assay was used to detect cell proliferation in MCF7 and MCF7TR cells seeded at 1,000 cells per well in a 96-well plate. MCF7 and MCF7TR cells were treated with brinzolamide (1 μM). Values are expressed as the mean ± standard deviation of three independent experiments. Samples t test; $^{**}p < 0.005$ and $^{***}p < 0.001$ were considered statistically significant.

(B) CCK-8 assay was used to detect cell proliferation in T47D and T47DTR cells seeded at 1,000 cells per well in a 96-well plate. T47D and T47DTR cells were treated with brinzolamide (5 μM). Values are expressed as the mean ± standard deviation of three independent experiments. Samples t test; $^{*}p < 0.05$, $^{**}p < 0.005$, and $^{***}p < 0.001$ were considered statistically significant.

(C) Brinzolamide inhibited *in vivo* tumor growth in MCF7TR xenograft mice. MCF7TR cells were inoculated into the mammary fat pads of nude mice. When tumors became

palpable, tumors were treated with vehicle (corn oil) or brinzolamide. Tumor growth was analyzed by measuring the tumor volume. Tumor volume (length × width) over time for each treatment group was monitored via caliper measurements. Error bars represent standard error of the mean. Significance is shown only for endpoint measurements. Samples t test; ***$p < 0.001$ was considered statistically significant.

(D) Mouse weights over time for brinzolamide-treated vs. vehicle group. Error bars represent the standard error of the mean.

(E) Photographs of mammary tumors for brinzolamide-treated vs. vehicle groups at the study endpoint. The ruler scale is millimeters.

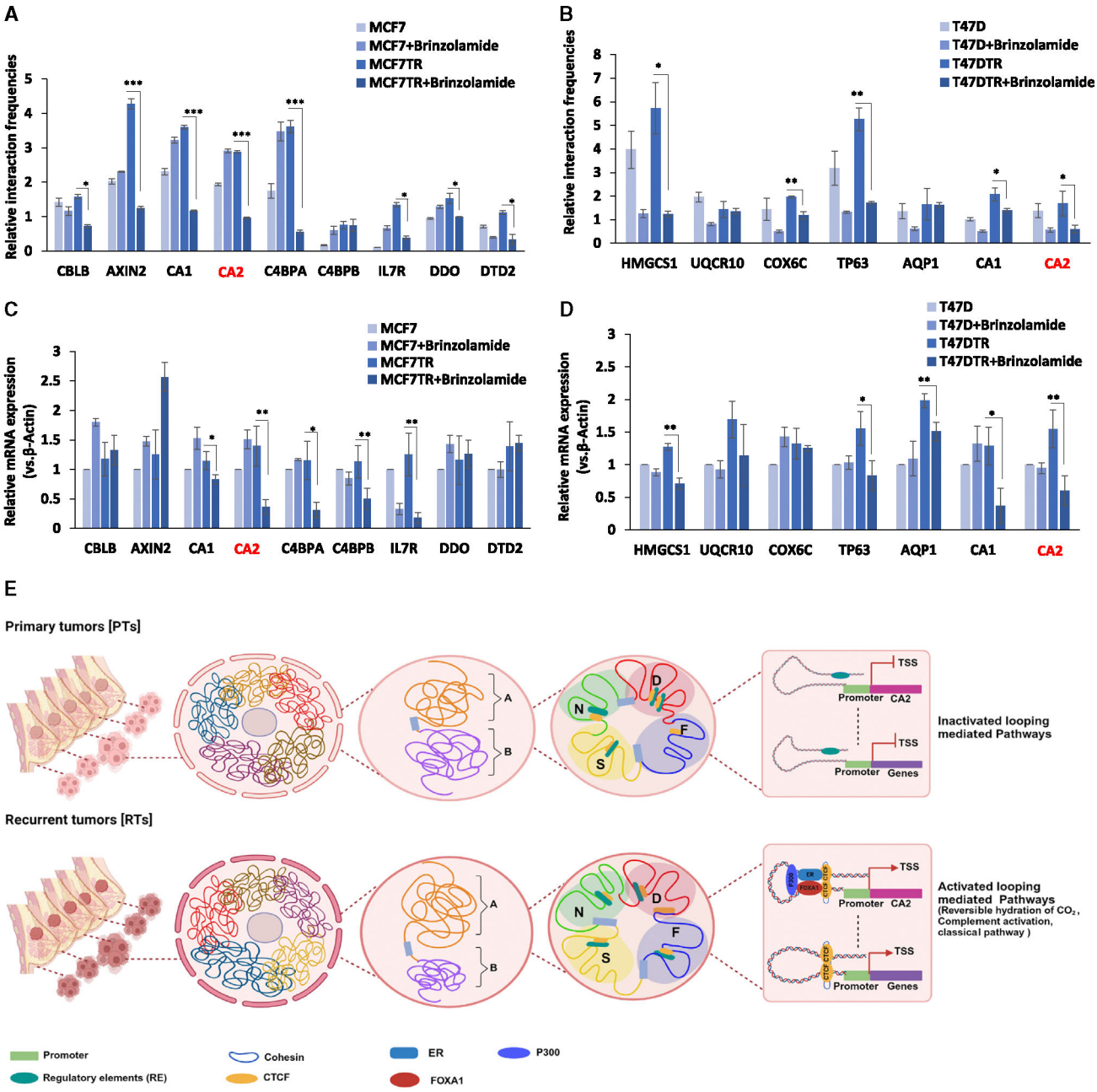

Figure 6. The inhibition of CA2 reverses chromatin looping

(A) Relative interaction frequencies of the selected genes in MCF7 and MCF7TR cells with and without brinzolamide identified by 3C-qPCR. Values are expressed as the mean ± standard deviation of three independent biological replicates; *$p < 0.05$, **$p < 0.005$, and ***$p < 0.001$.

(B) Relative interaction frequencies of the selected genes in T47D and T47DTR cells with and without brinzolamide identified by 3C-qPCR experiments. Values are expressed as the mean ± standard deviation of three independent biological replicates; *$p < 0.05$ and **$p < 0.005$.

(C) Quantitative real-time PCR was performed to detect the mRNA expression level of the selected genes in MCF7 and MCF7TR cells with and without brinzolamide. Values are expressed as the mean ± standard deviation of three independent biological replicates; *$p <$ 0.05 and **$p < 0.005$.

(D) Quantitative real-time PCR was performed to detect the mRNA expression level of the selected genes in T47D and T47DTR cells with and without brinzolamide. Values are expressed as the mean ± standard deviation of three independent biological replicates; *$p <$ 0.05 and **$p < 0.005$.

(E) A possible looping-mediated mechanistic model illustrating that inactivated biological pathways due to the weakened E-P looping in PTs became activated by enhanced looping activities in RTs, underscoring a role for chromatin looping in regulating downstream biological pathways and further driving the breast tumor heterogeneity of endocrine resistance.

KEY RESOURCES TABLE

REAGENT or RESOURCE	SOURCE	IDENTIFIER
RPMI1640 medium	Thermo Fisher Scientific	Cat# A1049101
Fetal bovine serum	Thermo Fisher Scientific	Cat# SH30071.03
Penicillin-Streptomycin	Thermo Fisher Scientific	Cat# 15140122
RPMI1640 medium	Thermo Fisher Scientific	Cat# 11835030
Charcoal stripped FBS	Thermo Fisher Scientific	Cat# 50-165-7328
Tamoxifen	Thermo Fisher Scientific	Cat# H7904-5MG
Power SYBRTM Green PCR Master mix	Applied Biosystems	Cat# 4367659
Formaldehyde	Fisher Scientific	Cat# BP531-500
Glycine	Fisher Scientific	Cat# A1381636
Protease inhibitor cocktail	Thermo Scientific	Cat# 78430
NEB buffer 2	NEB	Cat# B7002
SDS	Thermo Scientific	Cat# J1822036
Triton X-100	Thermo Scientific	Cat# A16046AE
HindIII	NEB	Cat# R3104
T4 DNA ligase	NEB	Cat# M0202
Proteinase K	NEB	Cat# P8107
RNase A	Invitrogen	Cat# 12091021
Phenol-Chloroform	Invitrogen	Cat# 15593049
Sodium acetate	Fisher Scientific	Cat# 60-024-24
SeaKem™ LE Agarose	Lonza	Cat# BMA50004
RIPA lysis buffer	Thermo Fisher Scientific	Cat#89900
BCA Protein Assay kit	Thermo Fisher Scientific	Cat#23225
PVDF membrane	Bio-Rad	Cat#1620177
Bovine serum albumin	Sigma	Cat#A9647
Inhibitors		
Brinzolamide	Selleckchem	Cat# S3178
Critical Commercial assays		
Proximo™ Hi-C kits v4.0	Phase Genomics	Cat# KT6040B
Cell Counting Kit-8 (CCK-8)	Dojindo	Cat# CK04-11

REAGENT or RESOURCE	SOURCE	IDENTIFIER
Quick -RNA™ Mini Prep	Zymo Research	Cat# R1054
High-capacity cDNA reverse transcription Kit	Applied Biosystems	Cat# 4368814
Western ECL Substrate	Bio-Rad	Cat#1705061
Biological samples		
Normal breast tissues	National Disease Research Interchange	N/A
Primary breast tissues	Bay Biosciences	N/A
Recurrent breast tissues	Bay Biosciences	N/A
Antibodies		
CA2	Proteintech	Cat# 16961-1-AP; RRID: AB_2065857
β-actin	Cell signaling	Cat# 4967S; RRID:AB_330288
Horseradish peroxidase conjugated Secondary antibody	Thermo Scientific	Cat# 656120; RRID:AB_2533967
Experimental models; cell Lines		
MCF7	Gift from Rachel Schiff lab	N/A
MCF7TR	Gift from Rachel Schiff lab	N/A
Oligonucleotides		
3C-qPCR Primers	Sigma-Aldrich	Method details
RT-qPCR primers	Sigma-Aldrich	Method details
Software and algorithms		
HiC-Pro	Servant et al 2015[22]	https://github.com/nservant/HiC-Pro
dcHiC	Chakraborty et al 2022[23]	https://github.com/ay-lab/dcHiC
TopDom	Shin etal 2016[24]	https://github.com/HenrikBengtsson/TopDom
Logomaker	Tareen et al 2020[65]	https://github.com/jbkinney/logomaker
GENOVA	van der Weide et al 2021[66]	https://github.com/robinweide/GENOVA
FitHiC2	Kaul et al 2020[26]	https://github.com/ay-lab/fithic
pygenometracks	Lopez-Delisle et al 2021[67]	https://github.com/deeptools/pyGenomeTracks
Bedtools	Quinlan etal 2010[68]	https://bedtools.readthedocs.io/en/latest/content/installation.html
DAVID	Dennis et al 2003[69]	https://david.ncifcrf.gov
Enrichr	Kuleshov et al 2016[30]	https://maayanlab.doud/Enrichr/
KM-plot	Lanczky etal 2021[70]	https://kmplot.com/analysis/

Cell Rep. Author manuscript; available in PMC 2025 May 24.

REAGENT or RESOURCE	SOURCE	IDENTIFIER
TADCompare	Cresswell et al 2020[71]	https://github.com/dozmorovlab/TADCompare
Python	Open source	Version 3.8.17
Code supporting this study	This paper	https://github.com/KunFang93/TumorSpecific3DChromatinDomain https://github.com/KunFang93/GISTA
GEO accession number	This paper	Database: [GSE261230]